UNIVERSITY OF CALIFORNIA
SANTA BARBARA

# ASIC-enabled High Resolution Optical Time Domain Reflectometer

A Thesis submitted in partial satisfaction
of the requirements for the degree

Master of Science

in

Electrical and Computer Engineering

by

Sandra Skendzic

Committee in charge:

Professor John E. Bowers, Chair

Professor Larry A. Coldren

Professor Luke S. Theogarajan

June 2015

The thesis of Sandra Skendzic is approved.

Larry A. Coldren

Luke S. Theogarajan

John E. Bowers, Committee Chair

June 2015

ASIC-enabled High Resolution Optical Time Domain Reflectometer



by

Sandra Skendzic

# Acknowledgements

I would like to thank Joe Ahadian, Charlie Kuznia, and the rest of the Ultra Communications family. I am extremely grateful to have been given this opportunity to work on an interesting and meaningful project. Everyone at Ultra Comm was incredibly supportive and helpful to my success in this work. I would like personally thank Joe Ahadian for providing invaluable guidance, mentorship, and expertise throughout the project.

I would also like to thank Professor John Bowers for helping me on this project, allowing me to join his research group here at UCSB, and pairing me with one of his PhD students, Mike Davenport. I have truly enjoyed working with Mike and learning from his expertise in the material. I found the research to be a great addition to my thesis. I would also like to express gratitude to the rest of my committee members, Professor Luke Theogarajan and Professor Larry Coldren, for joining me in my thesis.

Last but not least, I would like to thank my wonderful family – my mom, my dad, and my sister – for supporting me throughout my graduate studies.

# Abstract

ASIC-enabled High Resolution Optical Time Domain Reflectometer

by

Sandra Skendzic

Fiber optics has become the preferred technology in communication systems because of what it has to offer: high data transmission rates, immunity to electromagnetic interference, and lightweight, flexible cables. An optical time domain reflectometer (OTDR) provides a convenient method of locating and diagnosing faults (e.g. break in a fiber) along a fiber that can obstruct crucial optical pathways. Both the ability to resolve the precise location of the fault and distinguish between two discrete, closely spaced faults are figures of merit. This thesis presents an implementation of a high resolution OTDR through the use of a compact and programmable ASIC (application specific integrated circuit). The integration of many essential OTDR functions on a single chip is advantageous over existing commercial instruments because it enables small, lightweight packaging, and offers low power and cost efficiency. Furthermore, its compactness presents the option of placing multiple ASICs in parallel, which can conceivably ease the characterization of densely populated fiber optic networks.

The OTDR ASIC consists of a tunable clock, pattern generator, precise timer, electrical receiver, and signal sampling circuit. During OTDR operation, the chip generates narrow electrical pulse, which can then be converted to optical format when coupled with an

external laser diode driver. The ASIC also works with an external photodetector to measure the timing and amplitude of optical reflections in a fiber. It has a 1 cm sampling resolution, which allows for a 2 cm spatial resolution. While this OTDR ASIC has been previously demonstrated for multimode fiber fault diagnostics, this thesis focuses on extending its functionality to single mode fiber.

To validate this novel approach to OTDR, this thesis is divided into five chapters: (1) introduction, (2) implementation, (3), performance of ASIC-based OTDR, (4) exploration in optical pre-amplification with a semiconductor optical amplifier, and (5) conclusion. Thus, it begins by providing background, basic OTDR operation, overview of ASIC functionality, and past experiments done with the ASIC for multimode fiber. Chapter 2 begins the investigation of a high resolution OTDR for single mode fiber. A though explanation of how the OTDR ASIC operates is presented in this chapter, as well as details on the OTDR scheme that has been implemented. Chapter 3 analyzes the performance of the OTDR. Chapter 4 introduces a hybrid silicon semiconductor optical amplifier and discusses its theoretical implication on the OTDR in terms of improving receiver sensitivity. Lastly, a summary of the findings and discussion of other applications lie in Chapter 5.

# Contents

# Chapter 1

# Introduction

The introduction of the laser in the early 1960s sparked the development of optical communication systems [1,8]. Many engineers believed the laser to be a promising solution to the growing demand for high bandwidth data transmission; all that was needed was the appropriate medium to facilitate this optical transmission. In the late 1950s, Dr. Charles Kao proposed very pure glass as the dielectric waveguide for propagating light. After refining a process for the removal of impurities, low-loss fibers with attenuation of 0.2dB/km were achieved. Shortly after, these low-loss optical fibers enabled the implementation of an optical telecommunications infrastructure.

One of the key motivations for constructing fiber-based systems is its inherent capacity for high-speed data transmission over extended distances. The first fiber optic systems developed in 1975 were designed to operate at a wavelength of 0.8 μm and transmit data at 45 Mb/s [3]. From that point, there was a gradual change in wavelength from 0.8 to 1.3 and to 1.55 μm, the third generation of fiber optic communication, which reached a data rate of 2.5 Gb/s. In the late 1990s that there was a dramatic increase in system capacity enabling terabit data rates through

the use of wavelength division multiplexing[1] (WDM) and optical amplifiers [6]. In 2011, one of the highest reported data rates of 101.7 Tb/s was achieved over 165 km of fiber [7].

These technological advancements ignited the development of lightwave systems in both long- and short-reach applications in order to meet ever-increasing bandwidth requirements and exploit other advantages over electrical cables, such as low weight and immunity to electromagnetic interference [10-13]. Concurrent with the development of lightwave systems has come the need for a method of characterizing fibers. Fiber loss can be measured with a known light source and a power meter; however, this does not provide sufficient information for diagnosing the origin of loss in the fiber. An Optical Time Domain Reflectometer (OTDR), on the other hand, can resolve the precise location of faults along a fiber and determine the nature of the problem; it is the most widely used instrument for fiber diagnostics today [9].

Although commercial OTDR instruments do exist [16], they tend to be costly, bulky, and allow only the characterization of one fiber at a time. As a result, the installation and maintenance of densely populated fiber optic networks can be difficult and expensive. This thesis presents an implementation of an OTDR through the use of a compact and programmable ASIC. The OTDR chip measures 4.0×1.65 mm and fulfills the role of a tunable clock, pattern generator, precise timer, electrical receiver, and signal sampling circuit. This OTDR ASIC technology permits lightweight packaging and low power consumption. Furthermore, its compactness gives the option of placing multiple ASICs in parallel, which could ease the measurements of several fibers at once.

[1] Wavelength division multiplexing is the technique where information is carrier on optical signals of different wavelengths, combined together, and transmitted over a single fiber. Signals are separated again when they've reached their destination [2]. Multi-terabit transmission can be achieved with dense wavelength division multiplexing (DWDM).

## 1.1 Basic OTDR Operation

Figure 1.1 illustrates the key components of a standard optical time domain reflectometer. The laser block typically includes a laser diode driver, a laser diode, and an external modulator (if the laser is being externally modulated). The receiver block consists of a photodetector, electrical amplifier(s), and analyzing circuitry.

The fundamental operation of an OTDR is based on the detection and analysis of optical reflections due to impurities or imperfections in the fiber. During OTDR operation, narrow optical pulses are injected into a beam splitter, and then propagate down the fiber under test. As the signal comes across discontinuities along the fiber, a fraction of the light is reflected, and routed back through the splitter to the receiver. Based on the timing and amplitude of the reflected pulse, the location and type of fault in the fiber can be determined.

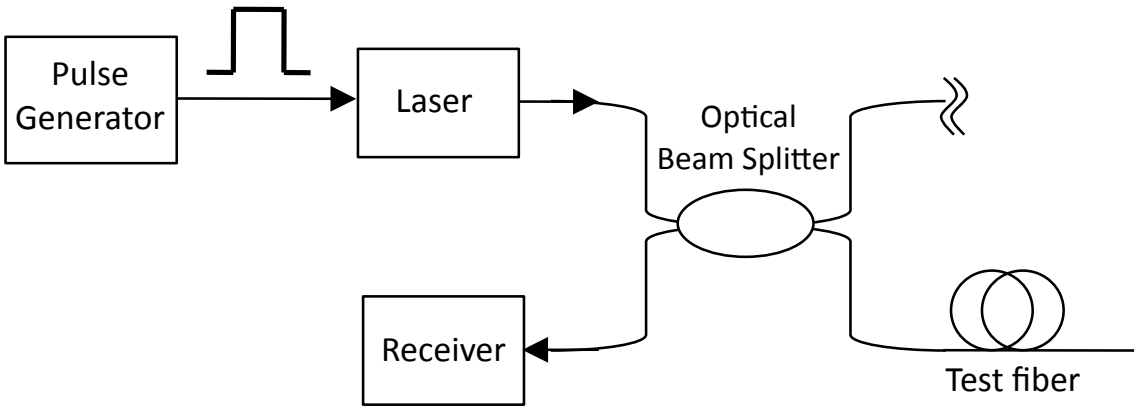


**Figure 1.1:** Simplified block diagram of a typical OTDR. Note that half the optical power is lost when it travels through the beam splitter; index-matching gel can be applied to one end of the splitter to suppress the reflection.

Reflections in the fiber occur whenever light experiences a change in index of refraction. The refractive index is defined as the ratio of the speed of light in vacuum to its velocity in the medium (Eq. 1.1). In single mode fiber, the optical mode extends well into the cladding,

and the amount of the mode that is carried by the cladding increases with wavelength. Furthermore, the density of fiber varies due to imperfections in the manufacturing process. As a result, the optical mode sees an effective index that depends on the mode profile and both the core and cladding indexes. It turns out that the refractive index for fiber glass is roughly 1.5. When light reaches the flat[2] cleaved end of a fiber, and transitions from the fiber glass core to air, 4% of the incident power is reflected back into the waveguide. The power reflection coefficient for this Fresnel reflection is shown in Eq. 1.2, where $n_{air}$ =1. Reflections can also arise from fiber connectors. Great effort has been put into different designs in order to minimize error when aligning two fibers; however, mechanical tolerances are not ideal, and residual air gaps can still exist. In some cases, the loss due to connectors is very low and does not appear as a reflective peak, but rather as a drop in the Rayleigh backscatter[3] level. Other typical causes of reflections in fibers are: fractures, mechanical splices, and a significant bend in the fiber.

(Index of refraction) $$n = \frac{c}{v} \tag{1.1}$$

where, $v = \text{speed of light in medium}$

$$\left|\Gamma\right|^2 = \left|\frac{n_{air} - n_{glass}}{n_{air} + n_{glass}}\right|^2 = \left|\frac{1-1.5}{1+1.5}\right|^2 = 0.04 = 4\% \tag{1.2}$$

[2] If the cleaved end is angled, some of the reflected light diverges at an angle outside the numerical aperture of the fiber, and does not make it back into the waveguide. Therefore, the total coupled reflection is less for angled cleaves than for flat cleaves.

[3] Rayleigh scattering is the phenomenon of light continuously scattering from tiny imperfections and impurities in the optical fiber as it propagates.

To locate the discontinuity in the fiber, the arrival time of the reflected pulse is divided by two (since it traveled twice the distance – there and back) and multiplied by the speed of light in the fiber (Eq. 1.3). The speed of light in a particular fiber is inversely proportional to the material's index of refraction, as shown by rearranging Eq. 1.1. Using Eq. 1.3, it is found that the time it takes for light to travel down 1 meter and back is approximately 10 nS (Eq. 1.4). This is an approximate relationship used throughout this thesis.

(Fiber fault location) $$d = \left(\frac{t_{arrival}}{2}\right) \cdot \left(\frac{c}{n}\right) \tag{1.3}$$

where,

$c = 3 \times 10^8$ m/s (speed of light in vacuum)
$n = 1.5$ (approximate index for glass)

(Roundtrip time to travel 1 m) 1 meter = 10 nS (1.4)

## 1.2 Unique Features of OTDR ASIC

ASIC technology has greatly advanced since the concept was first invented in 1948 [15]. In general, it has enabled high-density, high-speed applications, and now has paved the way for an innovative approach to OTDR: the integration of OTDR functionality on a single chip (Figure 1.2). Timing circuits, a pattern generator, receivers, and sampling circuits have all been condensed onto a die that measures 4.0×1.655 mm and 200μm thick [5,14]. When the ASIC is combined with a laser, a photodetector, and the right supplementary components, an OTDR

with 1 cm sampling resolution can be realized. This Section aims to summarize the unique features and capabilities that make up this OTDR ASIC.

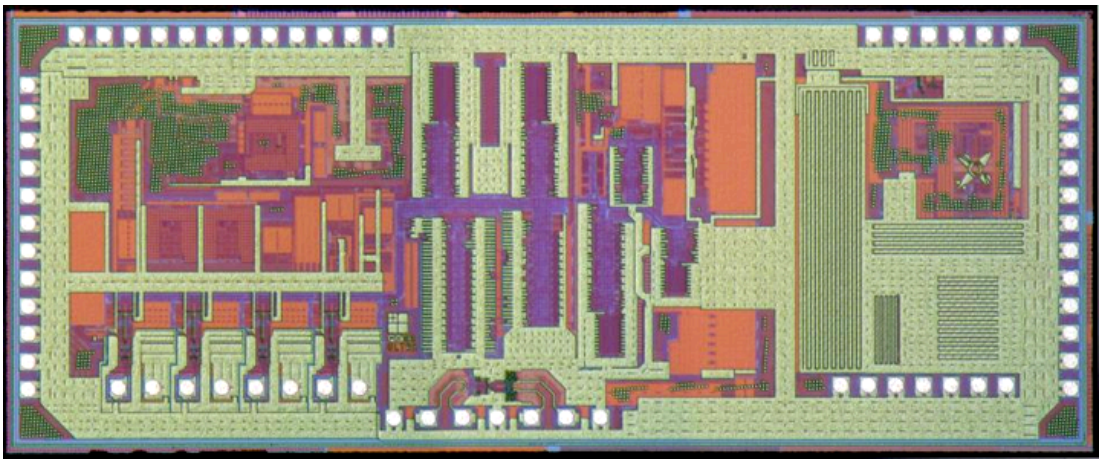


**Figure 1.2:** OTDR ASIC, from Ref. 17.

The OTDR integrated circuit (IC) is programmable and can be optimized for specific applications. Its clock synthesizer, which uses a 50 MHz reference clock, can generate a frequency from 1 to 5 GHz. The pattern generator consists of a 10-bit shift register that may be pre-loaded with any arbitrary pattern. Therefore, when operating at a frequency of 5 GHz, the OTDR logic can produce an outgoing pulse as narrow as 200 pS (full-width half-maximum). Figure 1.3 shows the output of the chip for a bit pattern of 0x001. The pulse width can be easily adjusted by setting a different bit pattern. For example, the bit pattern, 0x03f, produces a 1.2 nS wide pulse. In addition, the 10-bit shift register may be looped back on itself and inverted; this would produce a 20-bit pattern consisting of the 10 bits and their complements; an example is shown in Figure 1.4. The output patterns is driven off chip via a set of differential CML outputs; thus, the originally set pattern, or its complement can be selected. The tail current source of the differential pair can be adjusted to produce a CML output amplitude from ~200 mV to 425 mV.

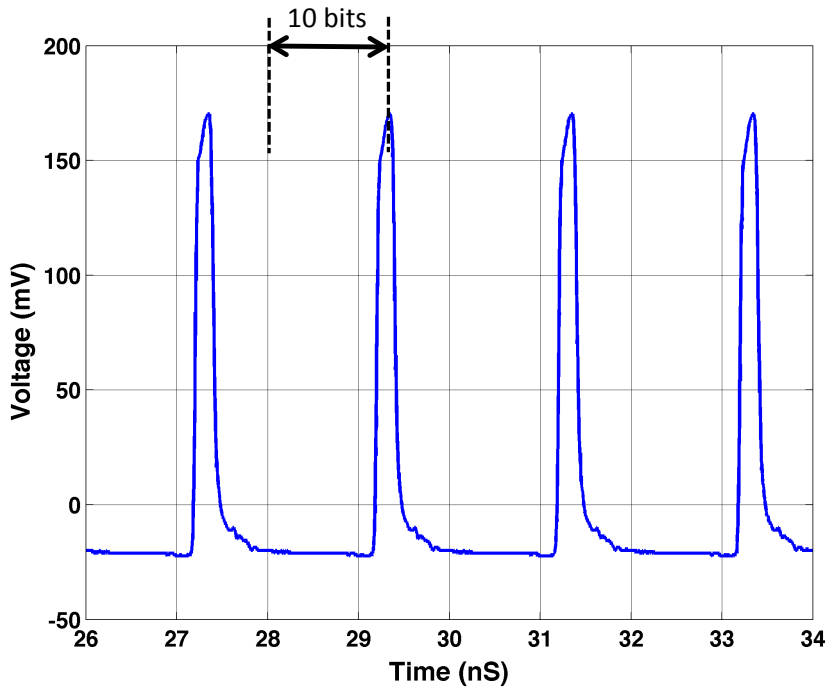


**Figure 1.3:** Electrical output of ASIC (ac coupled) with 10-bit pattern: 00000000001 (hexadecimal format: 0x001). The shift register is operating at 5 GHz, which produces a pulse 200 pS wide (FWHM). The amplitude of the pulse is 191.9 mV.

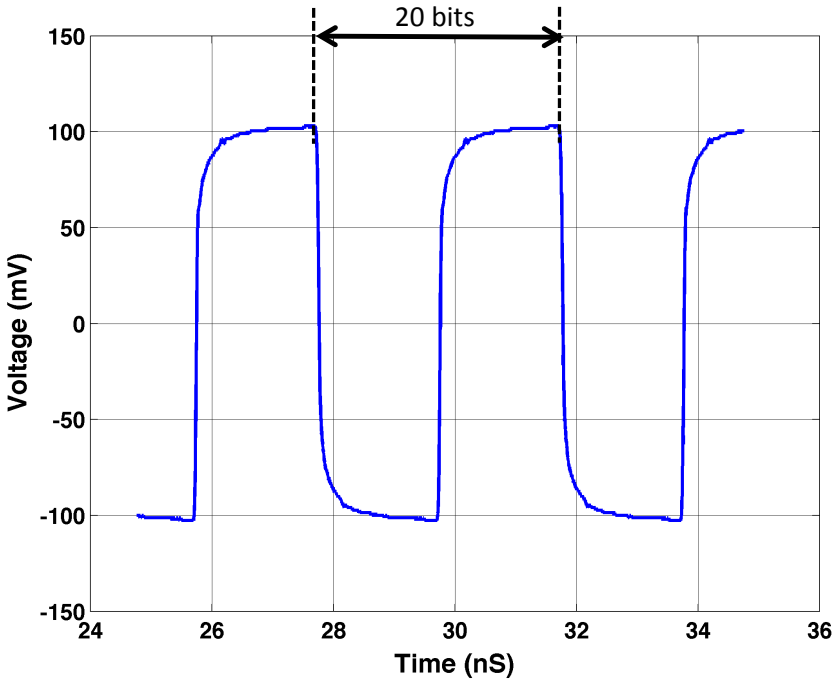


**Figure 1.4:** AC coupled electrical output of the ASIC with 10-bit pattern: 1111111111 (hexadecimal format: 0x3ff). The shift register is looped back on itself and inverted, thus producing a waveform with 50% duty cycle and 200 mV peak-to-peak. The period of the waveform is 20-bits long (~4 nS).

The OTDR receiver consists of a high-speed trans-impedance amplifier (TIA) and post amplifiers, a pair of track-and-hold circuits, and a back-end instrumentation section. Both the offset and gain of the TIA and post amplifiers can be tuned appropriately for detecting small or large signals. The track-and-hold circuits sample the amplified signal. The timing of the track-and-hold circuits is generated by two identical, independent count-down timers. The clock source to each counter may be independently shifted by half a clock cycle to provide an effective timing resolution of twice the clock rate. For example, at a clock frequency of 5 GHz, the sampling rate is 100 pS with the ½ clock delay, and thus provides 1 cm sampling resolution.

The entire receiver and sampling circuitry is repeated on the chip four times, which provides four different receiver channels. Multiple ASICs can be placed in parallel, which allows the characterization of parallel data links.

Lastly, a number of voltage and current sensors are mapped to critical analog output signals inside the IC in order to provide a built-in-test (BIT) measurement system. This is especially useful for verifying whether the chip is operating properly after adjusting settings, such as tuning the clock frequency or increasing the gain of the receiver.

| **Summary of OTDR ASIC Features** |
| --- |
| • Die size: 4.0×1.655 mm, 200 μm thick<br>• Operating temperature range: -40 to 120 °C<br>• Sampling resolution 1 cm (100 pS sampling rate)<br>• Internal clock generator: 1 to 5 GHz<br>• Internal 20-bit pattern generator<br>• Built-in-test (BIT) measurement system<br>• Four receiver channels<br>• Differential output amplitude: ~200 mV to 425 mV |

**Table 1.1:** Summary of OTDR ASIC features

## 1.3 Previous Progress with OTDR ASIC for Multimode Fiber

Previous testing shows the OTDR ASIC integrated within a fiber optic transceiver and used for characterizing multimode fiber [4]. Figure 1.5 shows the block diagram of the transceiver-OTDR integration. The transceiver is an 850 nm, VCSEL-based parallel-optic transceiver; it has four channels and is capable of 12.5 Gb/s data transmission. The output pattern generated by the ASIC is coupled to the laser diode driver (LDD) internal to the transceiver. During an OTDR measurement, a light pulse is produced and injected into the fiber via an integrated 50/50 optical beam splitter. The fraction of reflected light is passed through the splitter again and routed to a detector, which is connected to the sampling receiver of the OTDR ASIC. The four transmitter channels are linked with the four receiver channels of the OTDR ASIC. Thus, OTDR measurements can be made on four parallel transmit lines.

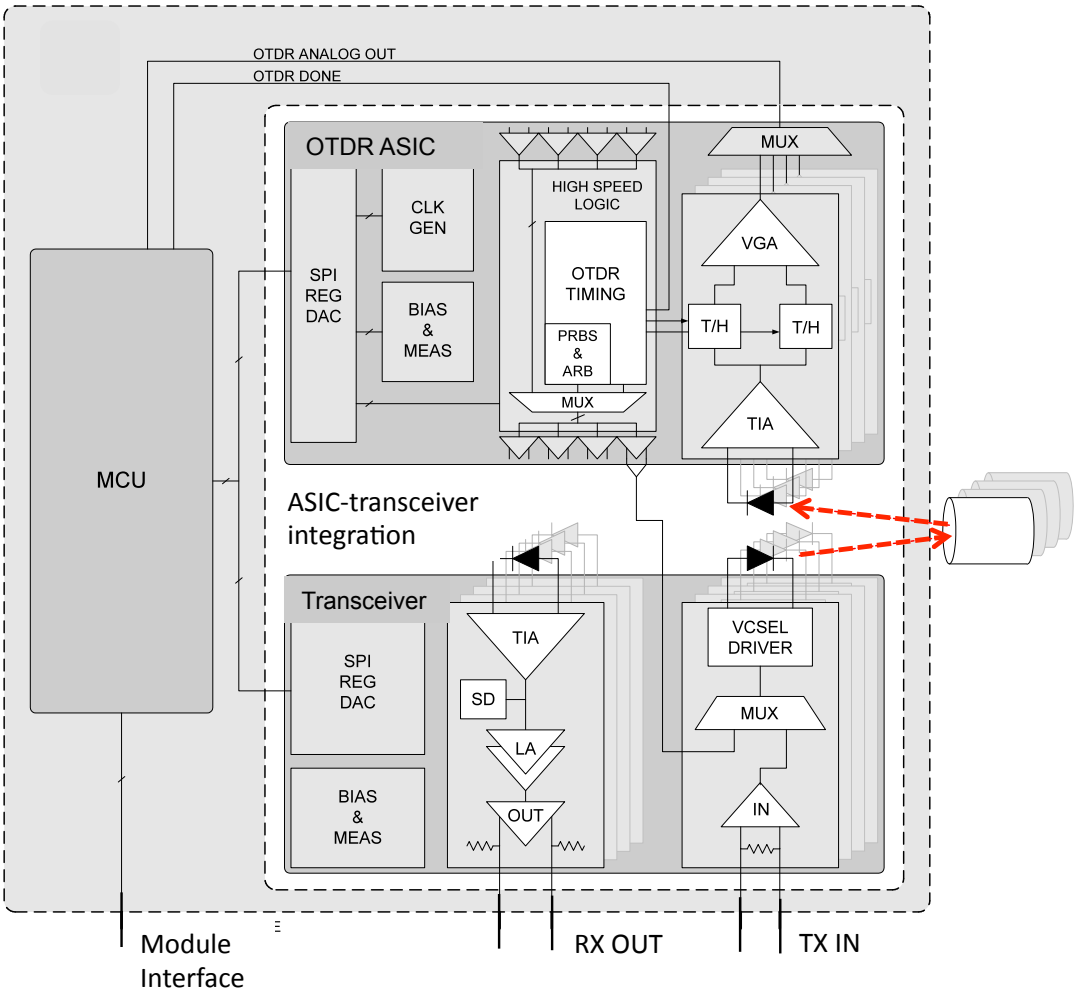


**Figure 1.5:** Block diagram of the OTDR enabled quad transceiver

The OTDR measurement was done on a MTP break-out cable (1 meter long) that was linked to the transceiver with a 25 cm long ribbon. The signal was detected with 1 cm sampling resolution. As shown in Figure 1.6, a reflection occurred at a surface discontinuity within the transceiver, at the MTP connector boundary (minor reflection), and at the cleaved end of the fiber (larger reflection).

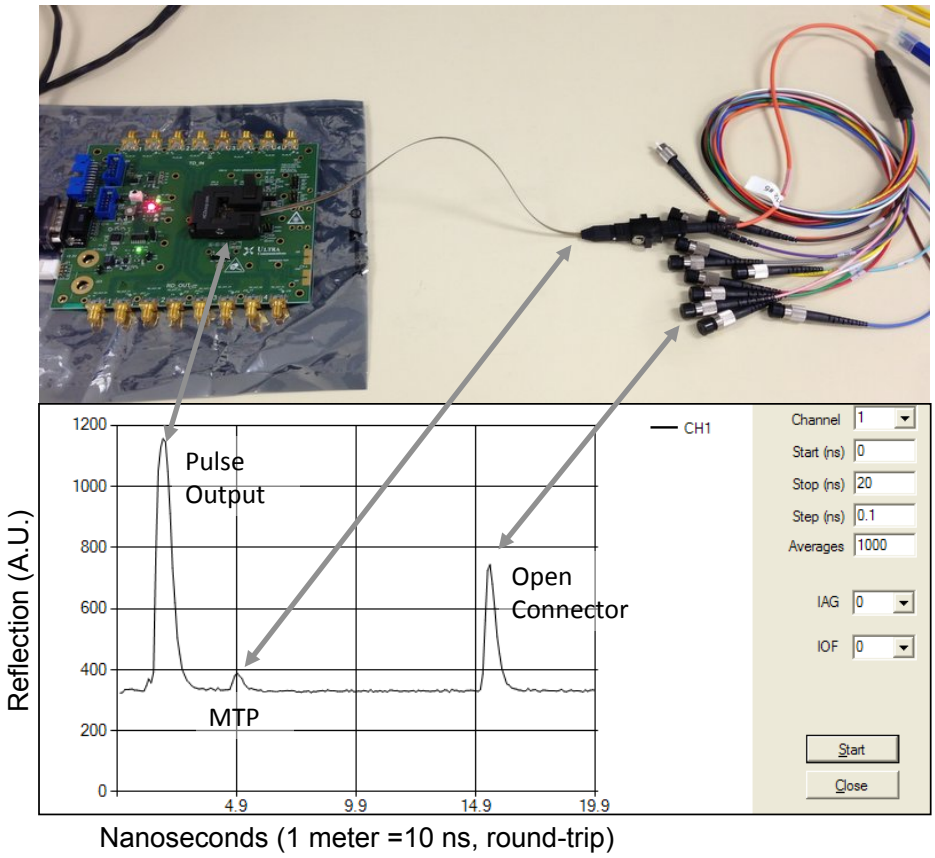


**Figure 1.6:** OTDR measurements with the parallel optic transceiver, from Ref 17.

Common faults in a fiber that cause reflections were measured. The cleaved end of the fiber (Fresnel reflection) showed a -14 dB back-reflection. A rough cut (done with scissors) caused -25.5 dB reflection. And significant bend causing the fiber to break resulted in -26.2 dB reflection. Furthermore, the root-mean-square (RMS) noise level of the receiver was measured to be 117 mV. By averaging 10,000 samples, the measured RMS noise level was reduced to 1.2 mV.

Overall, results were successful in demonstrating the integration of the OTDR ASIC within a 12.5 Gb/s transceiver and performing OTDR measurements on multimode fiber with 1 cm resolution. This thesis aims to extend the OTDR ASIC technology to single mode fiber fault diagnostics.

# References


[1] C. C. Davis and T. E. Murphy, "Fiber-Optic Communications [In the Spotlight]," *Signal Processing Magazine, IEEE,* vol. 28, no. 4, pp. 148-152, Jul. 2011. [Online]. Available: http://ieeexplore.ieee.org/stamp/stamp.jsp?tp=&arnumber=5888645&isnumber=5888632

[2] H. J. R. Dutton, "Wavelength Division Multiplexing," in *Understanding Optical Communications*, 1st ed. Research Triangle Park, NC: IBM Redbooks, 1998, ch. 9, pp. 411-412. [Online]. Available: http://www.redbooks.ibm.com/pubs/pdfs/redbooks/sg245230.pdf

[3] F. Idachaba, D. U. Ike, and O, Hope, "Future Trends in Fiber Optic Communications," in *Proc. World Congress on Engineering,* London, U.K., 2014. [Online]. Available: http://www.iaeng.org/publication/WCE2014/WCE2014_pp438-442.pdf

[4] C. Kuznia, J. Ahadian, D. Pommer, R. Hagan, P. Bachta, M. Wong, K. Kusumoto, S. Skendzic, C. Tabbert, and M. Beranek, "Novel High-Resolution OTDR Technology for Multi- Gbps Transceivers," in *Optical Fiber Communication Conference*. 2014, Optical Society of America. [Online]. Available: http://www.opticsinfobase.org/abstract.cfm?URI=OFC-2014-W1F.2

[5] Ultra Communications, Inc. [Online]. Available: http://www.ultracomm-inc.com

[6] R. Essiambre, and R. W. Tkach, "Capacity trends and Limitis of Optical Communication Networks," *Proceedings of the IEEE,* vol.100, no.5, pp.1035-1055, May 2012. [Online]. Available: http://ieeexplore.ieee.org.proxy.library.ucsb.edu:2048/xpl/articleDetails.jsp?tp=&arnumber=6170861&queryText=history+optical+fiber+communication

[7] J. Hecht, "Ultrafast fibre optics set new speed record," *New Scientist,* issue 2809, Apr. 2011. [Online]. Available: http://www.newscientist.com/article/mg21028095.500-ultrafast-fibre-optics-set-new-speed-record.html#.VVlJNWaFZRk

[8] V. Alwayn, "Fiber-Optic Technologies," in *Optical Network Design and Implementation,* Indianapolis, IN: Cisco Systems, Inc., 2004.

[9] D. R. Anderson, L. Johnson, and F. G. Bell, *Troubleshooting Optical-fiber Networks,* 2nd ed. San Diego, CA: Elsevier Academic Press, 2004.

[10] P. Pepeljugoski, F. Doany, D. Kuchta, L. Schares, C. Schow, M. Ritter, and J. Kash, "Data Center and High Performance Computing Interconnects for 100 Gb/s and Beyond," *Optical Fiber Communication and the National Fiber Optic Engineers Conference,* March 2007. [Online]. Available: http://ieeexplore.ieee.org/stamp

/stamp.jsp?tp =&arnumber=4348628

[11] X. Zheng, Y. Luo, J. Lexau, F. Liu, G. Li, H. D. Thacker, I. Shubin, J. Yao, R. Ho, J. E. Cunningham, and A. V. Krishnamoorthy, "2-pJ/bit (On-Chip) 10-Gb/s Digital CMOS Silicon Photonic Link," *IEEE Photonics Technology Letters,* vol. 24, no. 14, pp. 1260-1262, Jul. 2012. [Online]. Available: http://ieeexplore.ieee.org/stamp/stamp.jsp?arnumber=6216513

[12] E. Murphy, C. Michie, H. White, and W. Johnstone, "Power Saving Technique Suitable for DWDM-PON on Aircraft," *Avionics, Fiber-Optics and Photonics Conference,* pp 21-22, Oct. 2013. [Online]. Available: http://ieeexplore.ieee.org/stamp/stamp.jsp?tp=&arnumber=6661603

[13] G. M. Proudly et al., "Developing Aircraft Photonic Networks – An Overview of the European Daphne Project," *Avionics, Fiber-Optics and Photonics Conference,* pp 1-2, Oct. 2011

[14] J. F. Ahadian, C. B. Kuznia, R. T. Hagan, and R. J. Pommer, "Integrated optical time domain reflectometer," US Patent 8,854,609, Oct 7, 2014.

[15] D. R. Martinez, R. A. Bond, and M. M. Vai, *High Performance Embedded Computing Handbook: A Systems Perspective,* Boca Raton, FL: Taylor & Francis Group, 2008.

[16] "All Products Guide," vol. 3, Yokogawa Meters & Instruments Corp., 2011. [Online]. Available: http://tmi.yokogawa.com/files/uploaded/Catalog_YMI130_EN_1.pdf

[17] C. Kuznia, J. Ahadian, D. Pommer, R. Hagan, P. Bachta, M. Wong, K. Kusumoto, S. Skendzic, and C. Tabbert, "Novel High-Resolution OTDR Technology for Multi-Gbps Transceiver," presented at OFC conference, San Francisco, California, 2014.

# Chapter 2

# Implementation of High Resolution OTDR with ASIC

This chapter presents an implementation of a high resolution optical time domain reflectometer using the ASIC introduced in Chapter 1. First, the role of the ASIC in the OTDR system is described, including its internal hardware capabilities and its theory of operation. Section 2.2 provides details on the OTDR system as a whole, and on individual components external to the ASIC. This section also presents the results for an OTDR measurement. Section 2.3 derives a model for the optical receiver, which is later used for understanding certain performance parameters. Lastly, the OTDR performance is analyzed in Section 2.4.

## 2.1 OTDR ASIC Theory of Operation

The principal function of an OTDR is characterizing optical fibers by locating and diagnosing fault(s) along a fiber. This capability is based on measuring the amplitude and the arrival time of back-reflected light due to a discontinuity in the fiber. The OTDR ASIC includes most of the necessary functions for performing a measurement including: (1) clocking, (2) timing and pattern generation, (3) receiving, and (4) sampling. The key functions of the ASIC and the fundamental OTDR operation are illustrated in Figure 2.1.

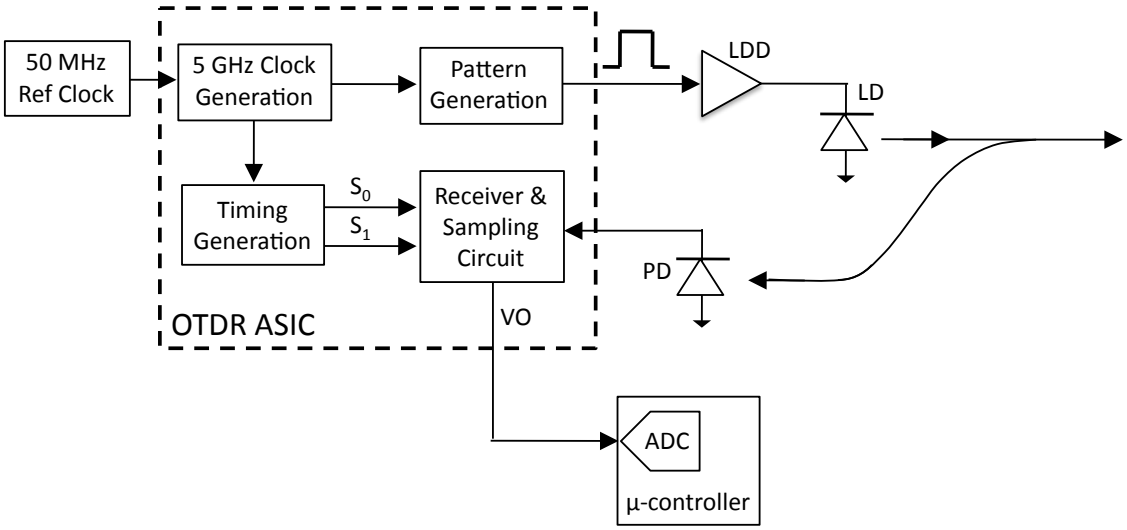


**Figure 2.1:** Basic OTDR ASIC functionality. Laser diode driver (LDD), laser diode (LD), photodiode (PD), and analog-to-digital converter (ADC) within the microcontroller.

When an OTDR cycle is triggered, the ASIC generates an electrical pulse that is converted to light with an external laser diode driver (LDD) and laser diode (LD). Concurrently, two different timing signals, $S_0$ and $S_1$, are generated and routed to the receiver block; these are the times at which the signal will be sampled for reconstructing the waveform. When the modulated light experiences a discontinuity, such as the cleaved end of the fiber, a fraction of the pulse reflects. The return signal is collected by a photodiode (PD) external to ASIC; the generated

photocurrent is transformed to voltage via the OTDR receiver circuit. The received signal is sampled at $S_0$ and $S_1$. Once the ASIC receiver is done sampling, the sample time $S_1$ is incremented by 100 pS, and another OTDR cycle is initiated. $S_0$ is held constant just before the test pulse to provide a fixed offset reading. This repeats until samples are acquired over the indicated time span. The output signal of the ASIC, $V_O$, is routed to the microcontroller and samples are digitized by the internal analog-to-digital converter (ADC). Essentially, the ASIC captures the signal in a similar way that a sampling oscilloscope operates [4]. Assuming the reflected pulse reaches the receiver at precisely the same moment each OTDR cycle, the signal appears periodic, and we can collect discrete points to reconstruct a waveform.

The ASIC includes hardware features that allow efficient repeated sampling at the same time delay. The samples can then be averaged in order to improve the signal-to-noise ratio (further discussed in Section 2.4.2). It does so by collecting a number of voltage samples (number of averages) at each time instance before incrementing $S_1$. Figure 2.2 depicts the general software flow of the ASIC. The total amount of times the pulse is launched into the fiber is: Total Cycles = (Number of Samples) × (Number of Averages).

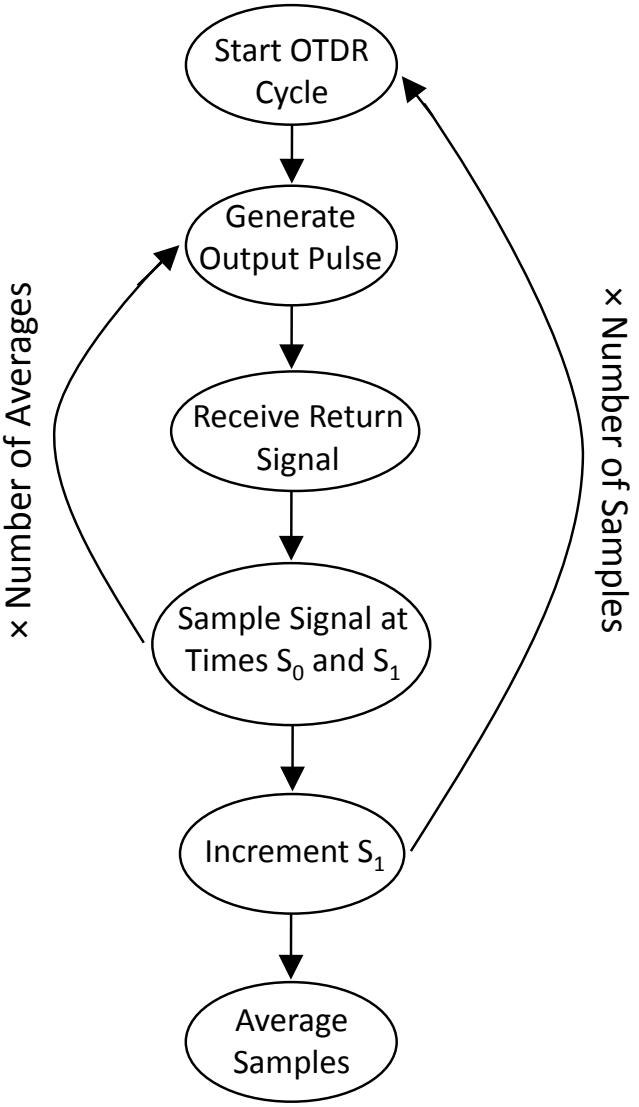


**Figure 2.2:** Software flow chart illustrating the operation of the OTDR ASIC during a measurement. $S_0$ and $S_1$ are the times the amplified back-scattered signal is sampled. $S_0$ is held constant just before the test pulse to provide a fixed offset value, while $S_1$ is swept.

The pulse width at the output of the receiver and the receiver sampling frequency determine the smallest distance that can be distinguished between two reflection peaks, also know as the measurement or spatial resolution. At minimum, the sampling rate should be twice the rate of the signal being sampled. This is to ensure that there are sufficient samples to accurately reconstruct the waveform (Figure 2.3).

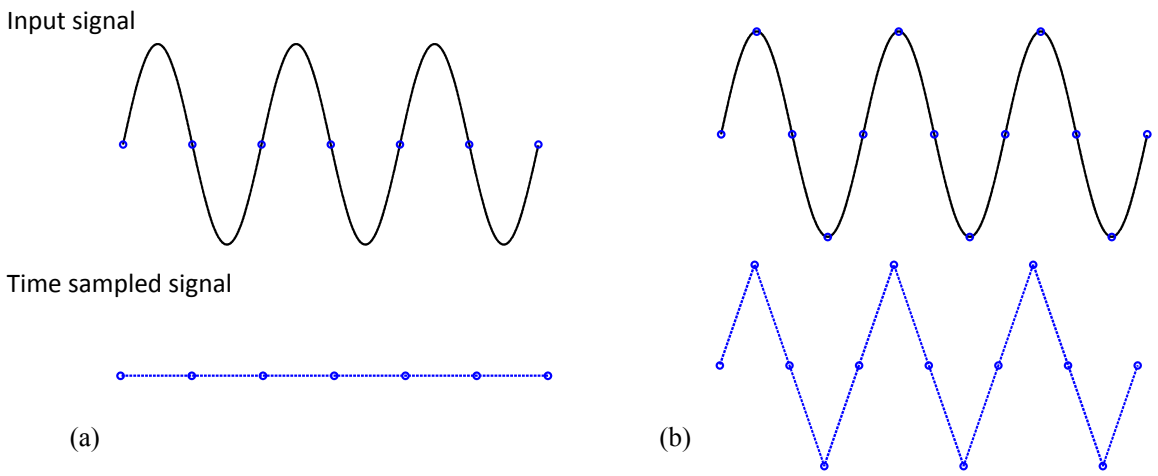


**Figure 2.3:** (a) Sampling at one times the frequency of the signal results in a misrepresentation of the signal. In this example, the regeneration of a sine wave looks like a DC signal. (b) When sampling at twice the frequency of the signal, the regeneration begins to approximate the sine wave.

In the case of the OTDR ASIC, the sampling rate of the receiver is 10 GHz (with the half-clock phase delay setting discussed in Section 1.2), which yields a sampling resolution of 100 pS. With this sampling resolution, the shortest pulse than can be resolved at the output of the receiver is 200 pS (FWHM). Since the FWHM is approximately equal to the two-point spatial resolution [2-3], the OTDR ASIC properties allow for 2 cm spatial resolution (Eq. 2.1). Note that we used the 10 nS = 1 m relation from Section 1.1.

(Spatial resolution) $$\left(200\text{ pS}\right)\left(\frac{1\text{ m}}{10\text{ nS}}\right)\left(\frac{1\text{ cm}}{0.01\text{ m}}\right)=2\text{ cm} \tag{2.1}$$

## 2.1.1 ASIC Receiver Settings

The ASIC receiver consists of an instrumentation amplifier with adjustable gain and offset; possible settings are summarized in Table 2.1. Although any combination of the two can be used, certain gain and offset settings may reach the limit of the receiver and cause the

receiver to clip at negative and/or positive voltages. For example, if the gain is increased in order to detect smaller signals, the offset should be raised as well to avoid voltage clipping on the bottom; however, if the gain is increased a great deal, then voltage clipping may occur at the top, distorting the signal. This section explores the various gain/offset pairs in order to prevent signal distortion in future OTDR measurements.

| **Gain Settings** | |
|---|---|
| Setting No. | Gain (V/V) |
| 0 | 1 |
| 1 | 2 |
| 2 | 3 |
| 3 | 4 |
| 4 | 5 |
| 5 | 6 |
| 6 | 8 |
| 7 | 11 |

| **Offset Settings** | |
|---|---|
| Setting No. | Offset |
| 0 | 300 mV |
| 1 | 400 mV |
| 2 | 500 mV |
| 3 | 600 mV |
| 4 | 700 mV |
| 5 | 800 mV |
| 6 | 900 mV |
| 7 | 1 V |

**Table 2.1:** OTDR instrumentation amplifier settings. Any combination of gain and offset can be selected.

The noise of the receiver is well approximated as a Gaussian random process, which is explained in Section 3.2; however, when voltage clipping at the receiver occurs, the noise distribution is skewed. The deviation from Gaussian was used as a measure of signal distortion. The noise of the OTDR receiver was measured by running an OTDR measurement for a large time span (to collect several thousand data points) without any optical signal coupled to the photodiode (same method discussed in Section 3.2). For a 960 nS time interval, 9,600 samples were collected. Figure 2.4 shows a 10 nS segment of the waveform and its corresponding noise distribution for three different gain/offset pairs. For gain = 0, offset = 0 setting, the noise distribution emulates the normal fit. When the gain was increased to the $7^{th}$ setting, the receiver was clipping at negative voltages. And with the gain = 7, offset = 7, the receiver was clipping at both negative and positive voltages.

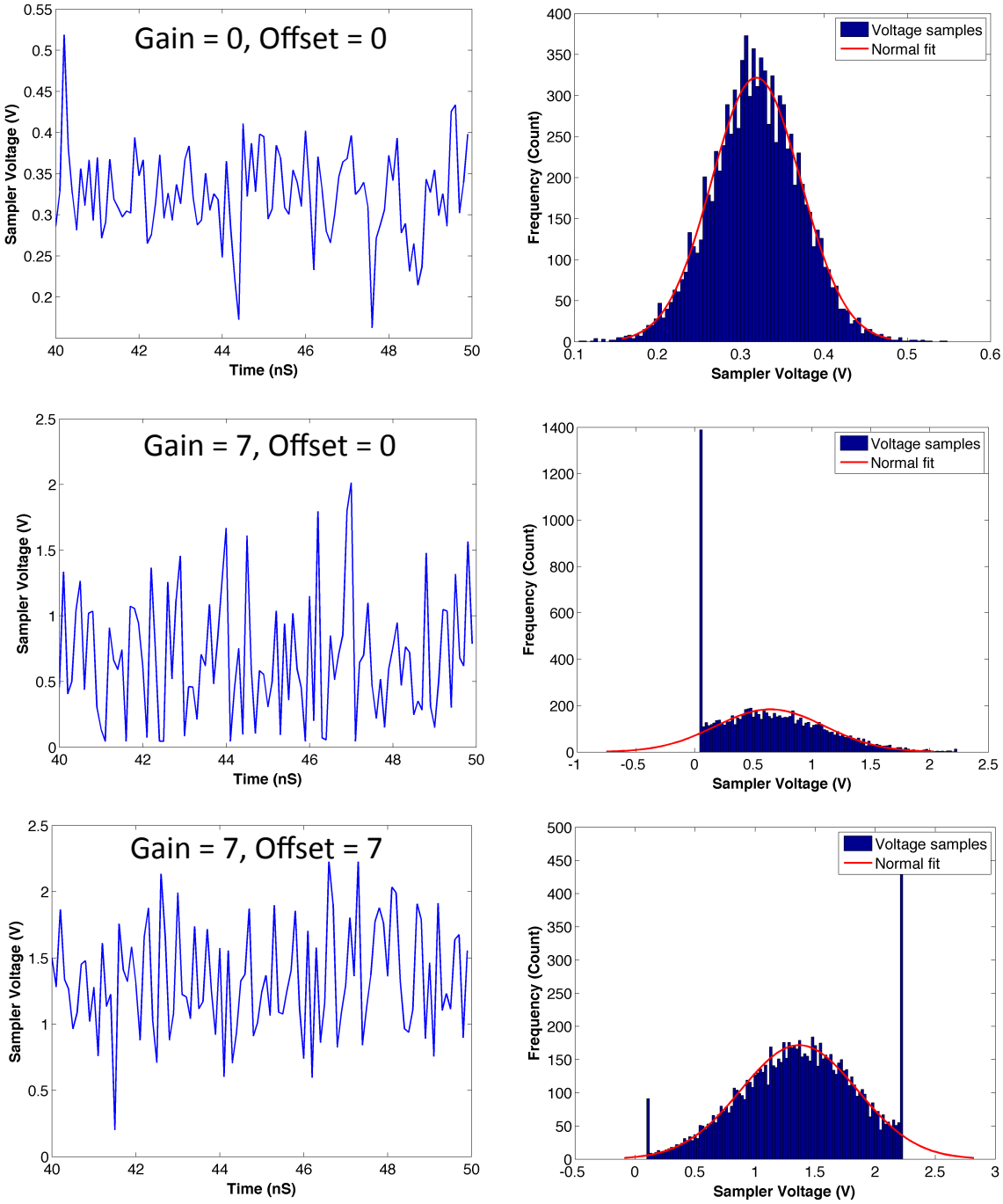


**Figure 2.4.** Sample waveforms (left) at the output of ASIC receiver for various gain/offset settings and their corresponding distributions (right). For gain = 7, offset = 0, the sample distribution shows voltage clipping at the bottom. For gain = 7, offset = 7, the distribution shows voltage clipping at the top and bottom.

For symmetric probability density functions (PDFs), such as a Gaussian distribution, the mean, median, and mode are ideally the same. In this particular context, the difference between the mean and median is a useful metric for quantifying the amount of signal distortion. If the receiver is saturating at the top or bottom, it will drive the counts upward at a single voltage "bin" of the histogram. As a result, the mean will change from that of a symmetric distribution, while the median will remain the same. Essentially, the median represents the true underlying signal level, but it is not used due to the inefficiency of evaluating it in real time on the small microcontroller[4]. Instead, the mean is used because it is easy to implement. The mean-median difference is then the error that is introduced by making this practical choice.

Figure 2.5 plots the mean-median error for each gain/offset combination setting[5]. At a given gain setting, the mean-median metric is first positive, which indicates that the noise is clipping at lower voltages. As the DC offset is raised, the bottom saturation is relieved and the mean-median approaches zero (hence the downward slope). After a certain point of raising the offset, the noise will begin to clip at the top, which results in negative mean-median values. The slope gets steeper with higher gain because increasingly amplified noise leads to excessive clipping at both the top and bottom; therefore, it deviates from the zero mean-median error faster.

Although gain settings 3 through 7 have a minimum error that occurs at a higher offset, it is likely that the receiver will saturate when a back-reflected signal is actually measured. The first three gain settings indicate fairly low errors, and are summarized in Table 2.2. It is seen that the optimal setting is gain = 0, offset = 0 with a mean-median of 0.03147 mV.

[4] The mean requires the ranking of data values, which is generally a slower process than computing the mean.
[5] The plots in Figure 2.5 actually show the linear fit for the measurements in order to illustrate the trends more clearly.

Going forward in this thesis, all measurements are made with this setting for the instrumentation amplifier in the ASIC receiver.

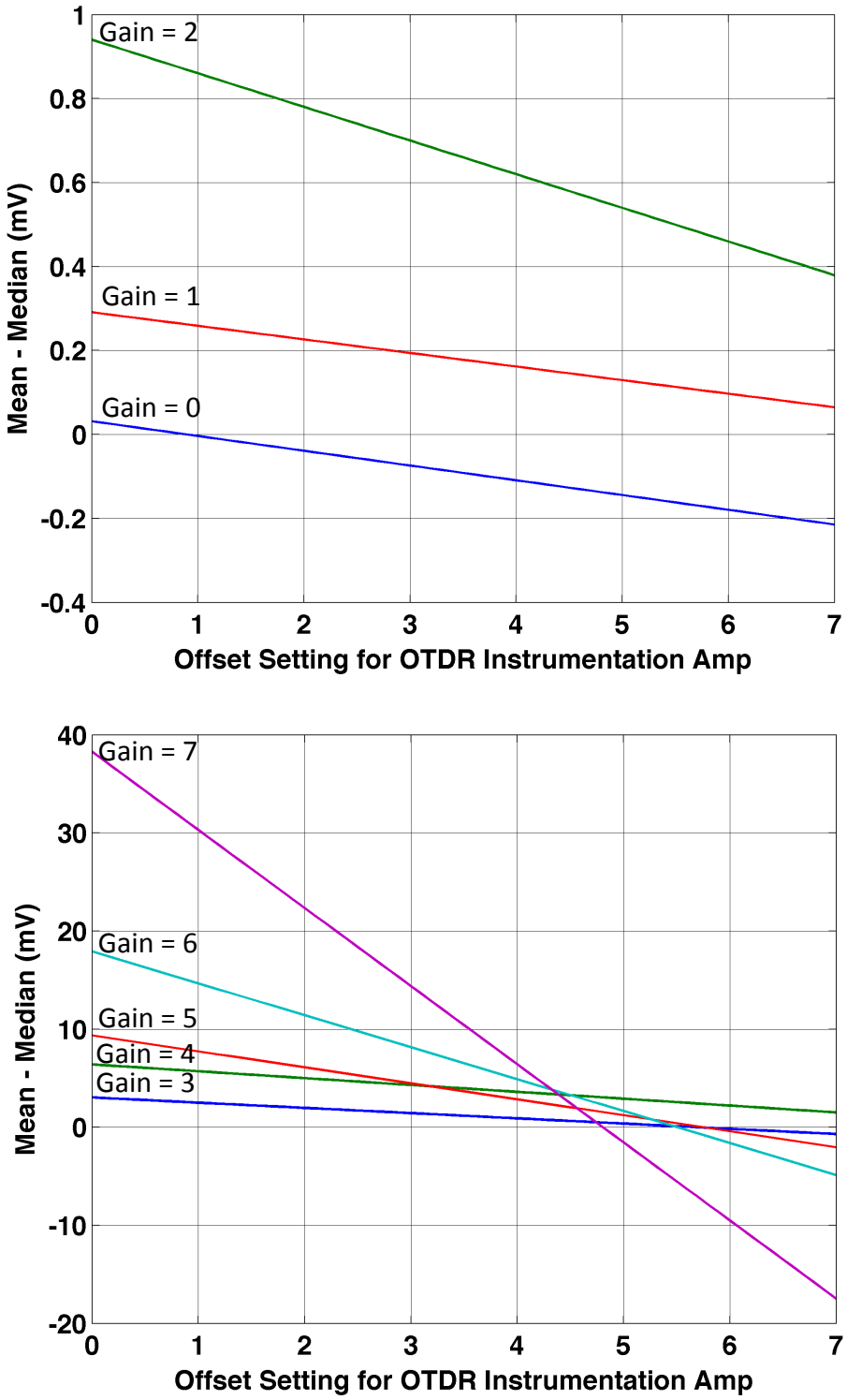


**Figure 2.5:** The mean-median error plotted for each gain/offset combination. Refer to Table 2.1 to map the setting number to its actual value. (i.e. offset = 0 corresponds to 300 mV)

| | Mean – Median Error (mV) | | |
|---|---|---|---|
| **Offset** | **Gain = 0** | **Gain = 1** | **Gain = 2** |
| 0 | 0.03147 | 0.2911 | 0.9406 |
| 1 | -0.02746 | 0.2587 | 0.8604 |
| 2 | -0.0864 | 0.2264 | 0.7803 |
| 3 | -0.1453 | 0.1941 | 0.7001 |
| 4 | -0.2043 | 0.1617 | 0.62 |
| 5 | -0.2632 | 0.1294 | 0.5398 |
| 6 | -0.3221 | 0.09705 | 0.4596 |
| 7 | -0.3811 | 0.06472 | 0.3795 |

**Table 2.2:** Summary of mean-median error for gain settings 0, 1, and 2

## 2.2 Proof of Concept

Chapter 1 presented a generic system diagram of an optical time domain reflectometer. Furthermore, in Section 2.1, the basic functionality of the OTDR ASIC, and its role in performing OTDR measurements, were discussed. In this section, a high resolution OTDR implemented with the ASIC is described. The OTDR experiment focuses on fiber fault measurements for single mode fiber.

### 2.2.1 OTDR System Architecture

The OTDR system consists of the OTDR chip, a laser diode driver, a laser diode, a 50/50 optical beam splitter, and a photodiode. A C8051 microcontroller by Silicon Labs [9] is used for priming the ASIC and controlling its functions. Matlab is used for interfacing with the microcontroller, and for processing the data. The system setup is shown in Figure 2.6. The OTDR system components (external to the ASIC) are summarized in Table 2.3.

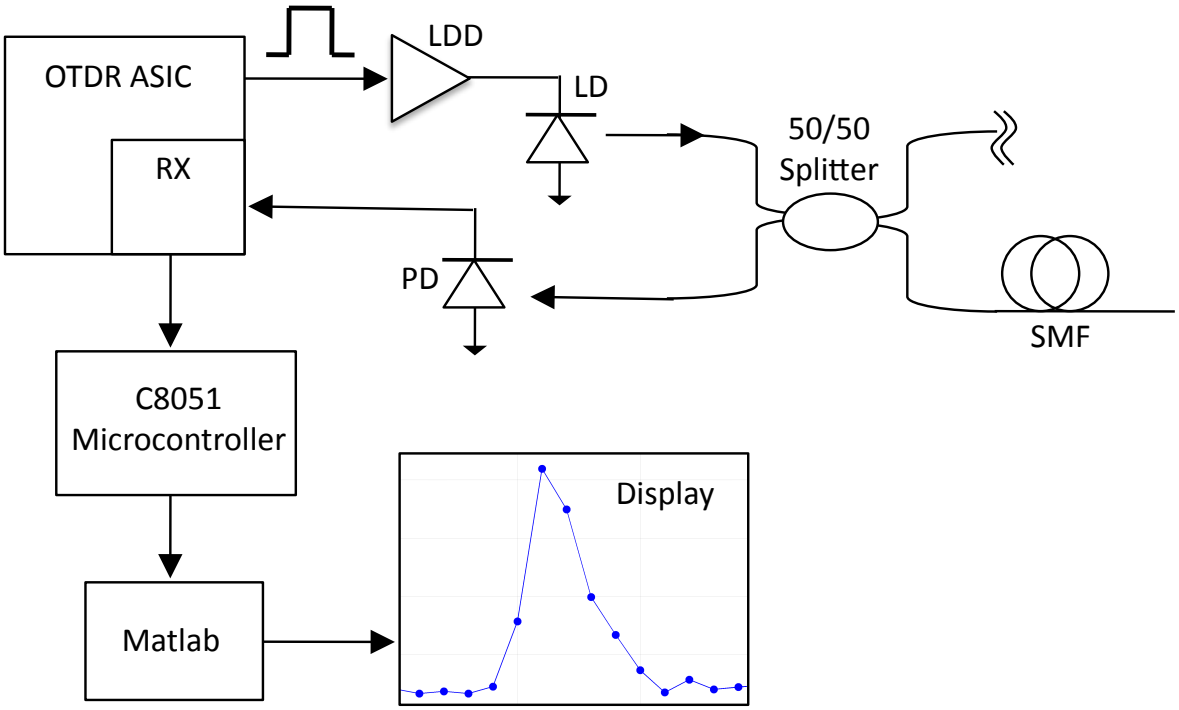


**Figure 2.6:** Block diagram of OTDR implementation with ASIC. Laser diode driver (LDD), Laser diode (LD), Single mode fiber (SMF), Photodiode (PD), and ASIC Receiver (RX). Index-matching gel is applied to one end of the splitter.

The laser used in this OTDR system was a commercial 1550 nm distributed feedback (DFB) laser [7]. The laser diode module comes in a 14-pin butterfly package with polarization maintaining optical fiber. The thermal electric cooler (TEC) and supporting heatsink is designed to maintain the device temperature at 25°. The dc light-current characteristics for the DFB laser were measured (Figure 2.7). The threshold current, $I_{th}$, is extracted from the intercept of the above-threshold curve and is found to be approximately 9.4 mA. The differential quantum efficiency, $\eta_d$, is 0.11 W/A, which is found by measuring the slope of the curve in the above-threshold regime.

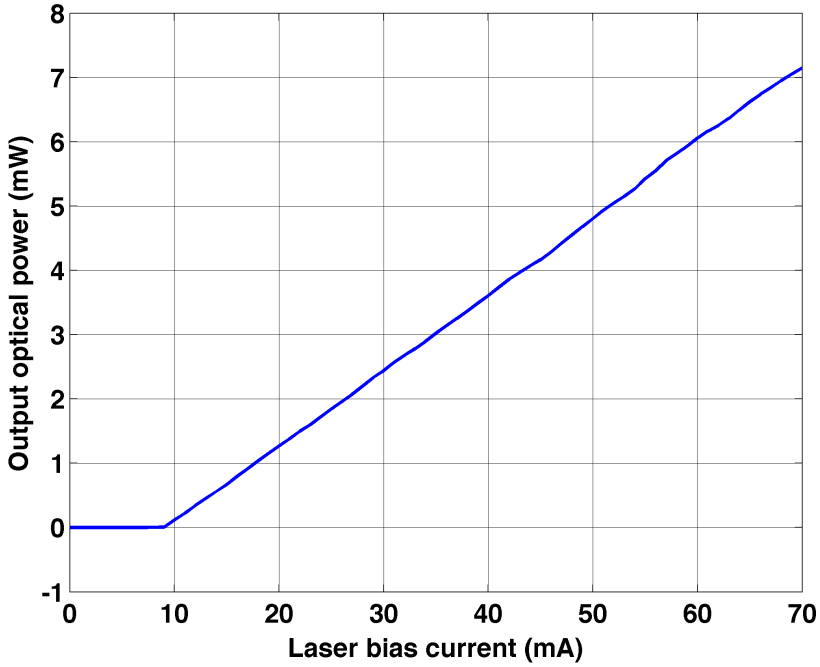


**Figure 2.7:** Measured output optical power per current injection for the 1550 nm DFB laser. The threshold current is approximately 9.4 mA. The differential quantum efficiency is measured to be 0.11 W/A.

The laser is directly modulated with a GaAs MMIC pHemt distributed driver amplifier, which comes in a 5×5 mm surface mount package and operates between DC and 20 GHz [8]. The amplifier is rated for 17 dB of negative gain and 8 Vpp saturated output swing into a 50 Ohm load. Gain flatness is +/-0.5 dB. Inputs and outputs are internally matched to 50 Ohms.

The back-reflected light is detected with an InGaAs PIN photodiode that comes in a coaxial package with optical fiber pigtail [6]. Measurements for generated photocurrent per optical input power are shown in Figure 2.8. The photocurrent is directly proportional to the incident optical power by a factor of the responsivity, $R_d$, which is extracted from the slope of the curve. The responsivity was measured to be 0.9050 A/W, which is within the specifications of 0.80-0.94 A/W.

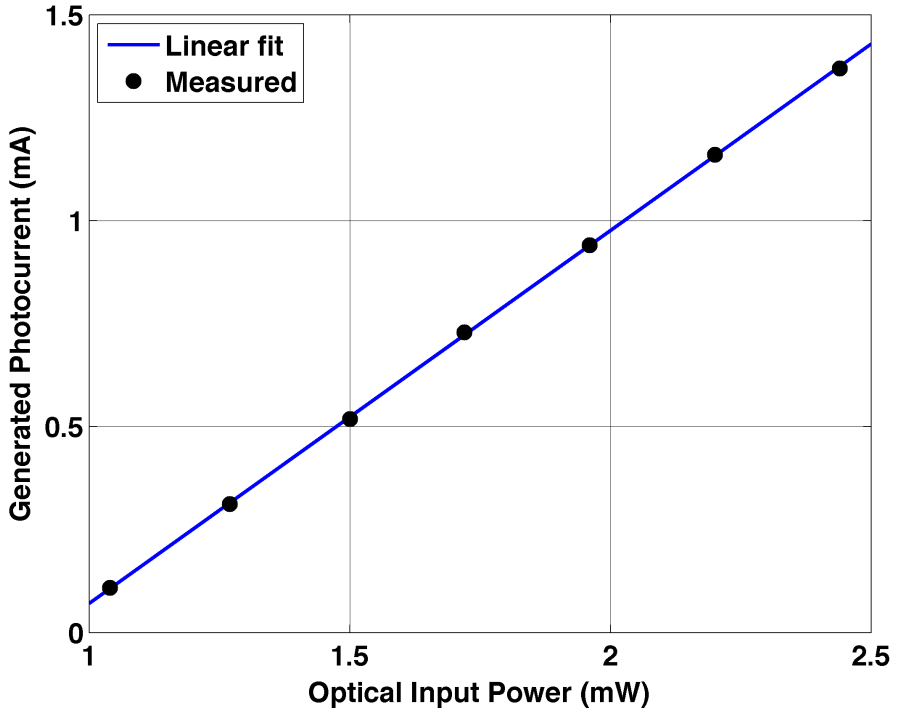


**Figure 2.8:** Measured PIN photodiode responsivity, $R_d$ = 0.9050 A/W

| **OTDR System Components** | |
|---|---|
| Laser diode driver | MZ Optical Modulator Driver by Hittite Microwave Corporation [8]<br>- Part No. HMC870lC5<br>- MMIC pHemt Distributed Driver Amplifier<br>- 5x5 mm surface mount package<br>- Operates between DC and 20 GhZ<br>- 17 dB negative gain<br>- 8 Vppk saturated output swing<br>- 5 V supply voltage, 140 mA supply current<br>- Input and output internally matched to 50 ohms |
| Laser | Distributed Feedback Laser (DFB) by Mitsubishi [7]<br>- Part No. FU-68PDF-V510MxxB<br>- 14-pin butterfly package<br>- Polarization maintaining optical fiber<br>- Monitor photodiode, built-in optical isolator, built-in thermo electric cooler (TEC) |

| | |
|---|---|
| | - 25 ohm input impedance<br>- Operating temperature: 25°C |
| Optical Splitter | 1310/1550nm 2x2 coupler with 50/50 splitter by Fiber Instrument Sales, Inc. [10]<br>- Part No. SDW13550222UC |
| Photodetector | PIN diode by NEC Laboratories America, Inc. [6]<br>- Part No. N47500 Series<br>- Coaxial package with an optical fiber pigtail<br>- Responsivity: 0.905 A/W<br>- Terminal capacitance: 0.7 pF at 25°C<br>- Reversed biased at 5 V |
| Microcontroller | Microcontroller by Silicon Labs [9]<br>- Part No. C8051F501<br>- 48-Pin QFP package<br>- 12-Bit ADC<br>- 3.3 Supply Voltage<br>- UART, SMBus, and SPI serial ports |

**Table 2.3:** List of components in the OTDR scheme (in addition to the OTDR ASIC)

## 2.2.2 Optical Pulse Generation

The OTDR signal path begins at the output of the ASIC, which puts out a 200 pS wide electrical pulse (FWHM). This is derived from a 10-bit pattern of all low bits and one high bit clocked out at 5 GHz. The bias current of the CML differential pair is adjusted to produce an amplitude of ~200 mV. The AC coupled positive output of the chip is shown in Figure 2.9.

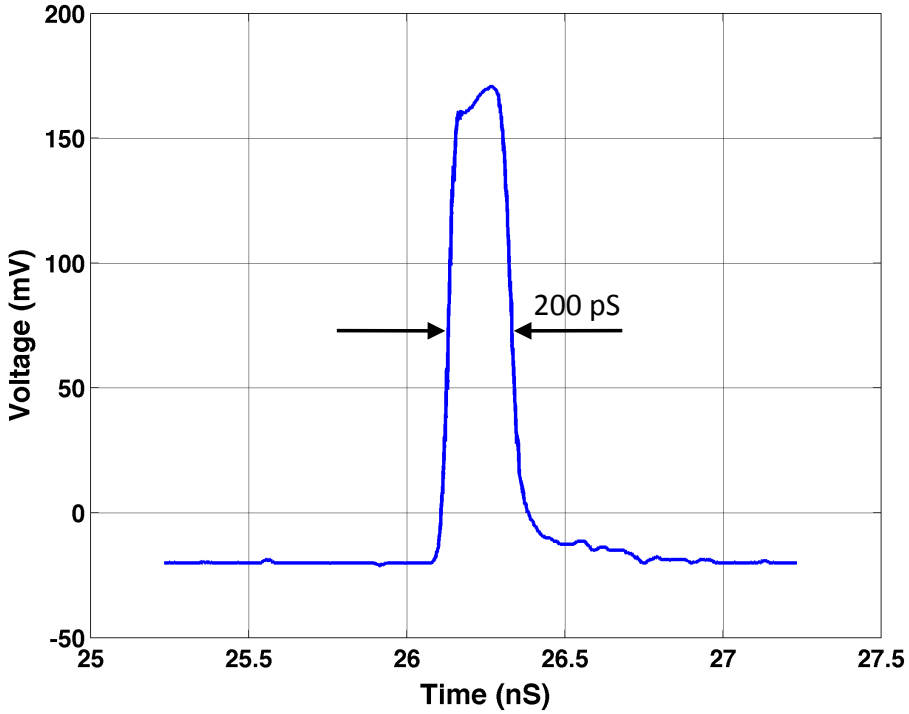


**Figure 2.9:** AC coupled output of OTDR ASIC. Bit pattern, 0x001, is clocked out at 5 GHz producing a pulse with full-width half-maximum of 200 pS. The amplitude of the pulse is 191mV.

There are two modulation techniques for generating an optical signal: direct modulation and external modulation. In the former case, the laser is biased close to its threshold and driven by an electrical bit stream that raises the current of the laser significantly above its threshold, thus creating optical pulses representative of the digital bit pattern. In the latter case, the laser is biased at a constant current to provide a CW light source, and an optical modulator is placed after the laser, which converts the CW light to an encoded light signal. The biasing of the optical modulator must be carefully regulated to maintain high optical extinction. To simplify the implementation, direct modulation was used in the OTDR system described here.

To implement direct modulation, the output of the ASIC is AC coupled to the optical modulator driver IC. The purpose of the driver is to modulate data on the fiber optic channel

by reducing or increasing current to the laser when the data bit is 0 or 1, otherwise known as modulation. The electrical output of the RF amplifier that modulates the laser is shown in Figure 2.10. The amplitude and negative gain are measured to be 1.478 V and 17.77 dB respectively. Note that the pulse is negative-going to match the polarity of the laser diode.

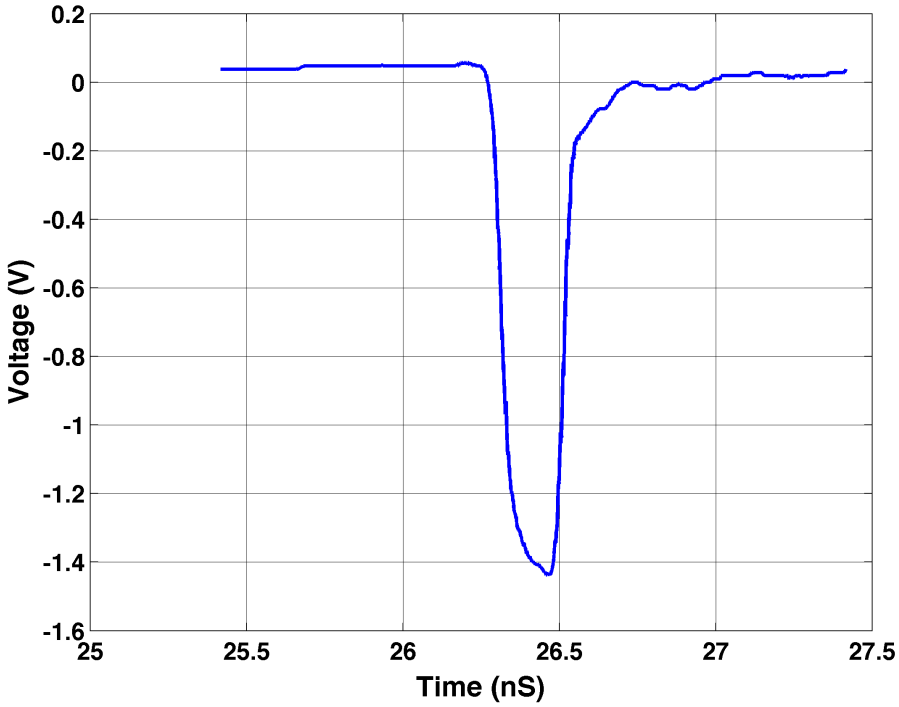


**Figure 2.10:** AC coupled output of the optical modulator driver with amplitude of 1.478 Vpp and FWHM of 200 pS.

The electrical pulse is coupled to a 50 Ω transmission line. The laser diode module, however, has an input impedance of 25 ohms. When the pulse signal encounters this impedance mismatch, it experiences a 33.3% reflection in voltage (Eq. 2.2). As a result, the amplitude of the driving pulse is actually 933 mV peak-to-peak (Eq. 2.4). Because the pulse is traveling from a higher resistance to a lower resistance, the transmitted pulse remains negative and the reflected pulse is inverted and becomes positive. The current reflection

coefficient is the same, but opposite sign; hence, the driving current amplitude is ~37 mA peak-to-peak (almost four times the lasing threshold).

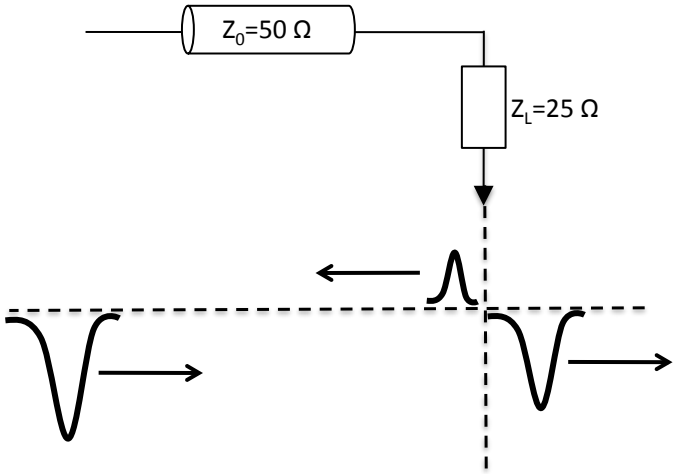


**Figure 2.11:** Signal reflection and transmission due to impedance mismatch at laser driver-laser diode interface

(Voltage reflection coefficient) $$\Gamma_V = \frac{(25-50)\ \Omega}{(25+50)\ \Omega} = -0.333 \quad (2.2)$$

(Current reflection coefficient) $$\Gamma_i = 0.333 \quad (2.3)$$

(Transmitted voltage amplitude) $$(1\text{-}0.333)(1.4\text{ V}) = 933\text{ mV} \quad (2.4)$$

(Transmitted current amplitude) $$\left(1+0.333\right)\left(\frac{1.4\text{ V}}{50\ \Omega}\right) = 37.3\text{ mA} \quad (2.5)$$

A 12.5 Gb/s (8.5 GHz) Picometrix fiber optic receiver module was used to view the generated optical pulse[6]. Figure 2.12 shows the resulting pulse with the laser biased just below threshold at 8 mA and driven with a 37 mA pulse of current. Notice that the pulse has

[6] The Picometrix has an offset of ~24 mV and a linear gain relationship until it saturates at higher input powers. In order to remain within the linear region of the receiver and avoid signal distortion, the optical signal was detected after it had already undergone a reflection at the cleaved end of the fiber and traveled through the splitter twice (total attenuation of ~22dB).

a FWHM of 60 pS, which is shorter than the 200 pS driving pulse. This is due to the evolution of the photon and carrier densities during the time when a current pulse is applied to a laser biased below threshold. When the current pulse is first applied, the injected carriers build up the carrier density up to a level slightly above the lasing threshold condition [5]. The time it takes to reach this threshold is the laser's turn-on delay. At this point, the carrier density is very high and causes the photon density to rapidly rise, which causes the carrier density to deplete. Thus, the photon density decreases. This process would continue until stabilization is reached. Instead, the current pulse has ended at this point, resulting in an optical pulse shorter than the electrical pulse[7]. The ripples at the end of the pulse are an artifact of the laser's relaxation oscillation caused by a rapid change in gain.

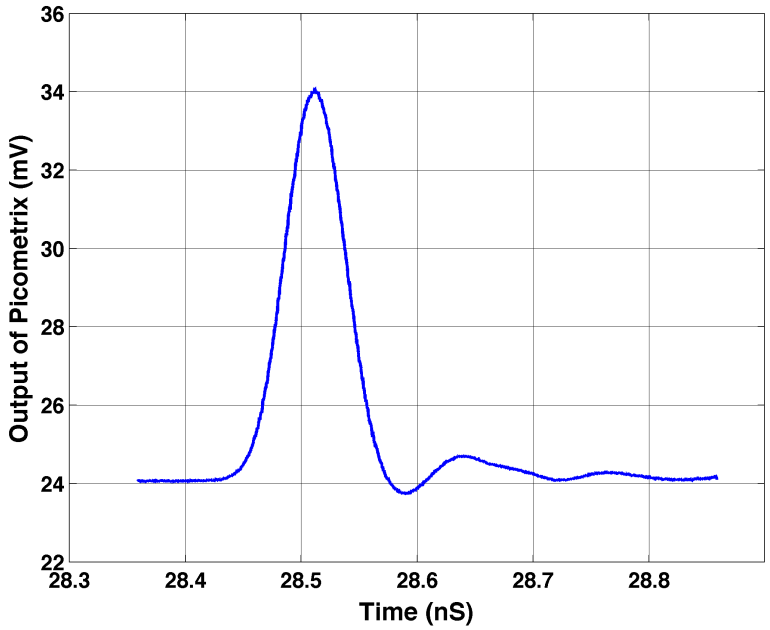


**Figure 2.12:** The optical pulse reflection from the cleaved end of the fiber displayed on high-speed oscilloscope[8] using the Picometrix fiber-optic receiver module. The optical pulse has a FWHM of approximately 60 pS.

[7] This mechanism is known as gain-switching. It has been shown that the shortest optical pulse is achieved when the laser is biased just below threshold [20].

[8] The scope is a digital communication analyzer (DCA) wideband sampling oscilloscope with a trigger bandwidth of DC to 3.2 GHz. It is the 86100 DCA model by Keysight Technologies.

## 2.2.3 OTDR Measurement

Experimental OTDR measurements were carried out based on the 4% Fresnel reflection that occurs at the cleaved end of the fiber. Figure 2.13 shows an OTDR measurement with the peak voltage occurring at 39.1 nS. The pulse has an amplitude of 252.3 mV and FWHM of ~300 pS. The test fiber was a 30 cm-long SMF patch cable. From another measurement (Figure 2.14), it is known that the reflection off the end of the optical beam splitter occurs at 36.1 nS (3 nS earlier). Using the approximate relationship, 10 nS = 1 meter (Eq. 1.2), it is found that the location of the reflection is 30 cm past the end of the optical beam splitter, which is in fact, the length of the fiber patch cable (Eq. 2.6).

(Event location)
$$\left(3\ \text{nS}\right)\left(\frac{1\ \text{m}}{10\ \text{nS}}\right)\left(\frac{1\ \text{cm}}{0.01\ \text{m}}\right)=30\ \text{cm} \tag{2.6}$$

The ringing at the beginning of the OTDR signal trace is due to transient electrical coupling occurring on the test board. This does not affect the measurement because it occurs much earlier in time than the reflective event. Ultimately, only the reflective events that occur after 36.1 nS (past the end of the splitter) are of interest.

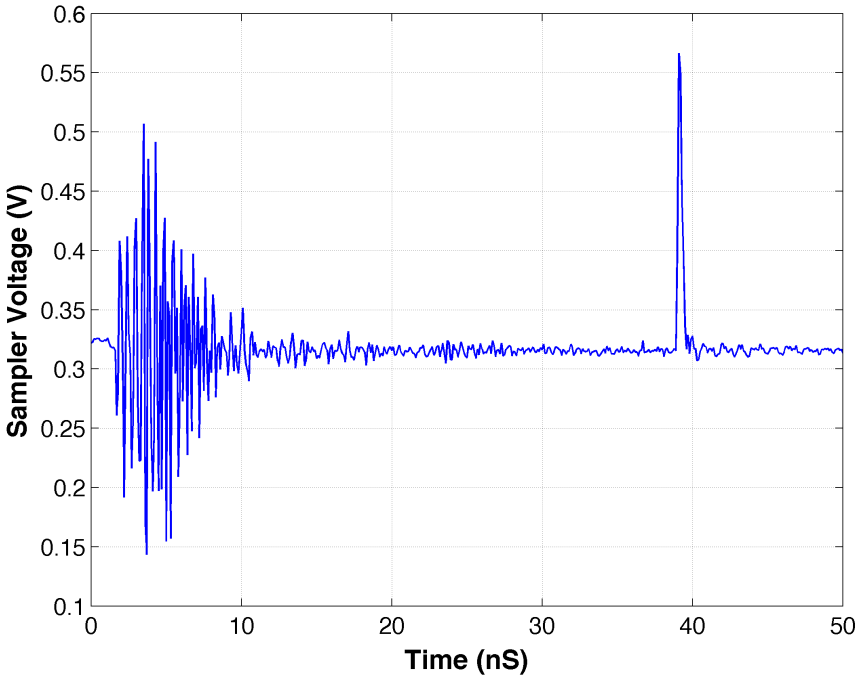


(a)

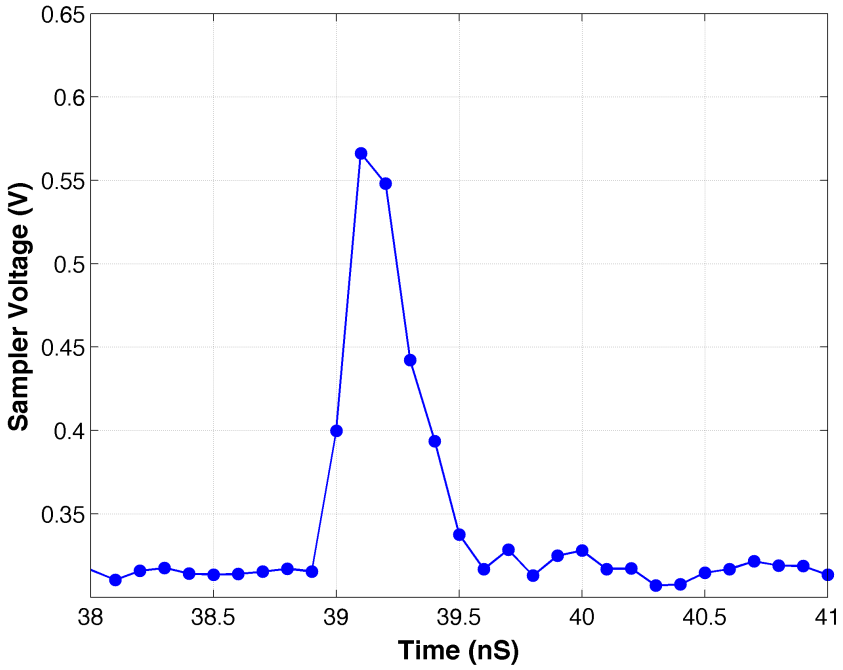


(b)

**Figure 2.13:** OTDR measurement with 1000 averages and sampling resolution of 1 cm. Laser was biased just below threshold at 8 mA. The amplitude of the reflection is 252.3 mV and the FWHM is ~ 300 pS. (a) Time span 0-50 nS (b) Time span 38-41 nS

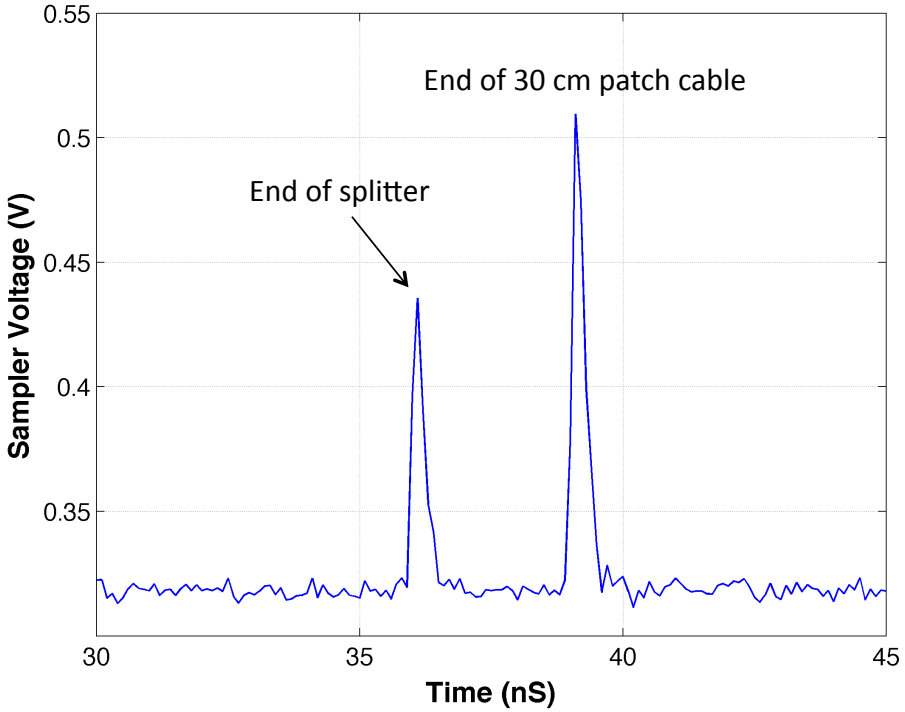


**Figure 2.14:** OTDR measurement from both ends of the optical beam splitter. One end has a 30 cm patch cable attached to it. The difference in amplitudes may be due to the splitter not be being a perfect 50/50.

## 2.3 Model for Optical Receiver

The optical receiver of the OTDR system consists of the OTDR ASIC receiver circuit and the external PIN photodiode. This section derives a model for the optical receiver that captures its gain and frequency response and can be used for analyzing performance parameters in later sections. First, the DC gain component is found by inputting a long, steady optical pulse and observing the amplitude of generated voltage at the output of the receiver. Then, the receiver's response to a short pulse is examined to estimate it as the impulse response of the receiver. The DC gain and the frequency response together comprise an approximate model for the optical receiver.

## DC Gain

The DC gain of the optical receiver can be expressed in units of Volts per Watts (V/W). This describes how much voltage will result when an AC optical signal is imposed on the detector. The gain of the optical receiver is determined by first looking at the optical output while it was pulsing periodically and finding the ratio of the voltage amplitude ($V_{amp}$) to the average voltage ($V_{avg}$) during one period. Then, the average generated photocurrent from the periodic pulse signal is measured. Knowing that the average generated photocurrent is proportional to its amplitude by the amount $\frac{V_{amp}}{V_{avg}}$, the amplitude of generated photocurrent, $I_{amp}$ can be calculated. Lastly, the gain Volts per Amperes (V/A) is calculated from the ratio of the voltage amplitude at the output of the ASIC receiver to the amplitude of the photocurrent. The gain in (V/W) is found by multiplying by the photodiode's responsivity, which is in units of (A/W).

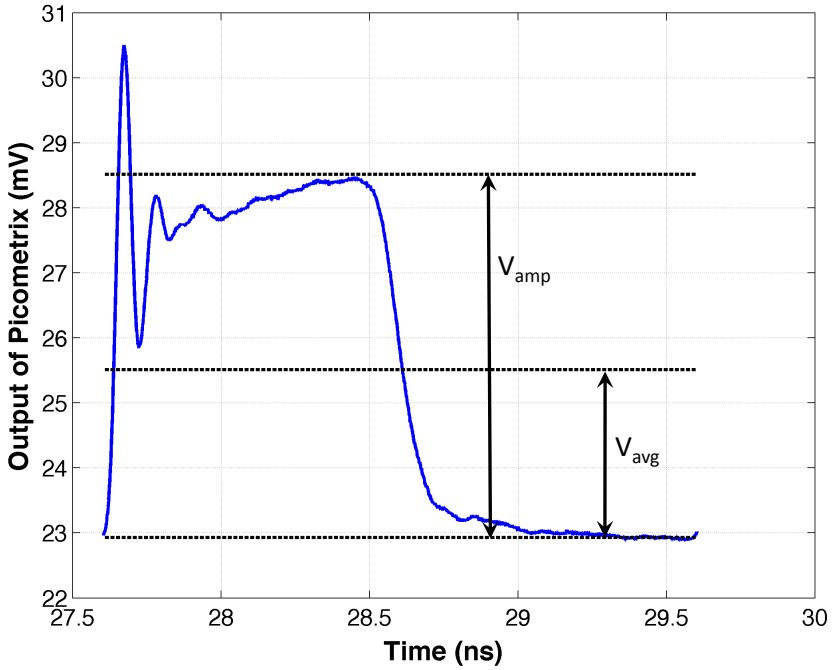


**Figure 2.15:** One period of the optical waveform, modulated with bit pattern: 1111110000 (hexadecimal format: 0x03f). Signal is displayed on high-speed oscilloscope using the Picometrix optical receiver module. The amplitude-to-average ratio is 2.164.

The long optical pulse was viewed using the Picometrix receiver module once again (Figure 2.15). The laser was biased at 40 mA (for lower relaxation oscillations from the laser) and modulated with the following bit pattern: 1111110000. The driving pulse was elongated to 6 bits (approximately 1.2 nS FWHM) to allow for it to settle after any transient response. The peak-to-average ratio is 2.164 (Eq. 2.7).

(Peak-to-average ratio)
$$\frac{V_{amp}}{V_{avg}} = \frac{5.5865\ \text{mV}}{2.5819\ \text{mV}} = 2.164 \tag{2.7}$$

An air-gap attenuator was placed right before the photodiode to vary the amplitude of the optical signal shown above. Figure 2.16 plots the output voltage amplitude against the input amplitude. The ASIC receiver begins to saturate at approximately 300 mV with an input of

12.9 μW; the maximum output voltage amplitude is approximately 400 mV. A linear fit for input powers below 12.9 μW indicates that the optical receiver has a DC gain of 20,805 V/W. With the PIN responsivity of 0.905 A/W, the gain is 22,989 V/A (or 85.5 dBΩ).

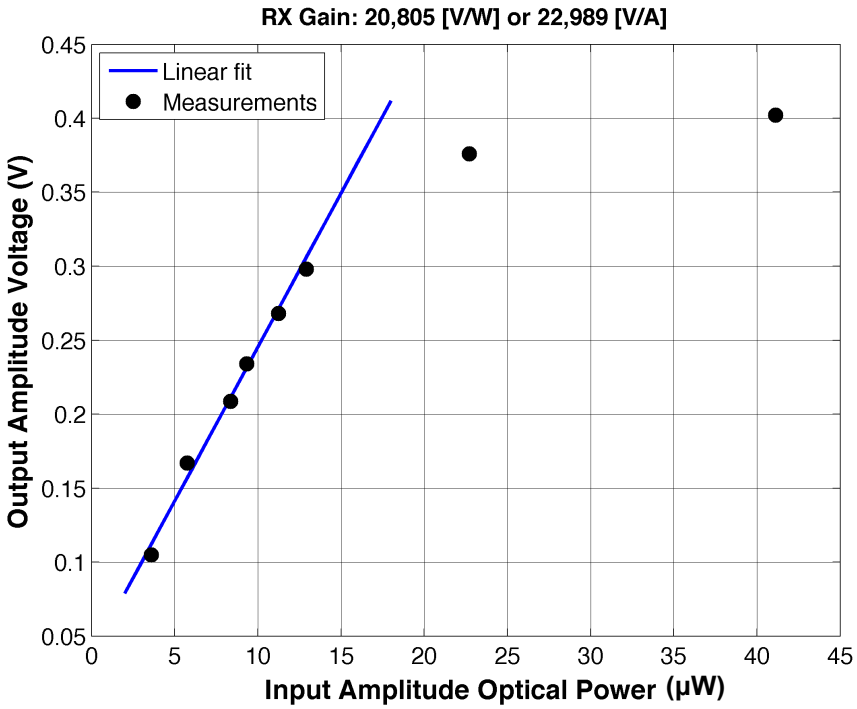


**Figure 2.16:** Plot for voltage amplitude at the output of the ASIC receiver versus optical power amplitude at the input of photodiode. Data is related to amplitude of generated photocurrent by the photodiode's responsivity. From the linear fit, a gain of 20,805 V/W is calculated.

## Frequency Response

Next, the frequency response of the optical receiver is characterized. In Section 2.2.2, the optical pulse just before the PIN diode is seen to be approximately 60 pS wide (FWHM). And, in Section 2.2.3, the pulse at the output of the ASIC receiver is seen to be ~300 pS; it is presented in Figure 2.17 again for convenience. The broadening of the pulse is due to the receiver bandwidth. Provided that the input pulse is sufficiently fast compared to the receiver's bandwidth, the output signal can be interpreted as the receiver's impulse response. The frequency response can be determined by taking the Fourier transform of the impulse

response. Figure 2.18 shows the frequency response of the optical receiver computed with the FFT built-in Matlab function[9]. It has an effective bandwidth of 1 GHz. Using the time-bandwidth product for a Gaussian shaped pulse [1], the minimum input rise time that is within the bandwidth budget is 350 pS (Eq. 2.9).

$T_r$ = Rise time of impulse response
$\Delta f$ = Bandwidth of RC circuit
0.35 = Gaussian pulse shape factor

(Time-bandwidth product) $$T_r \cdot \Delta f = 0.35 \tag{2.8}$$

$$T_r = \frac{0.35}{1\ \text{GHz}} = 350\ \text{pS} \tag{2.9}$$

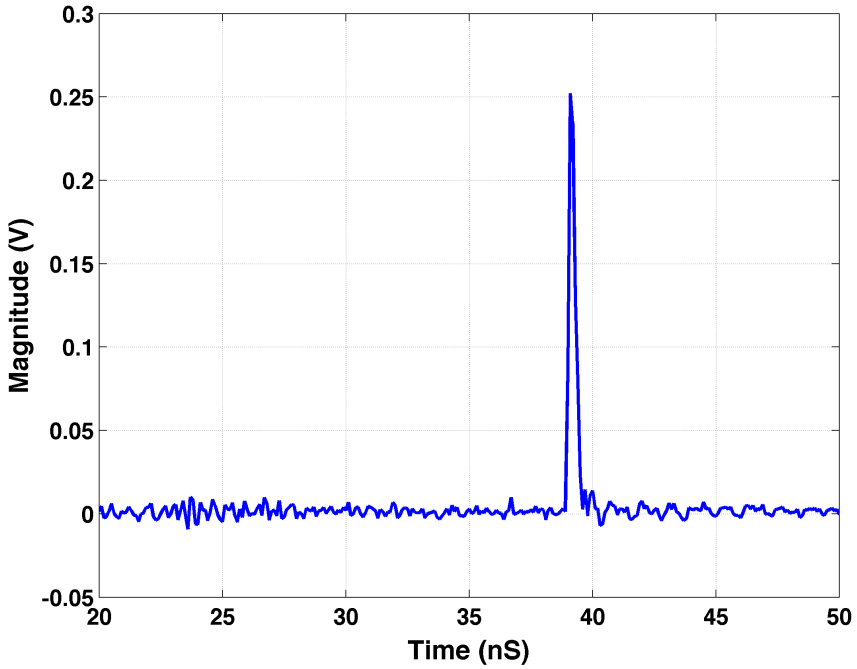


**Figure 2.17:** OTDR measurement approximating the impulse response of the receiver. The DC offset has been subtracted off.

[9] The FFT built-in Matlab function returns the discrete Fourier transform of a vector, computed with a fast Fourier transform algorithm [11].

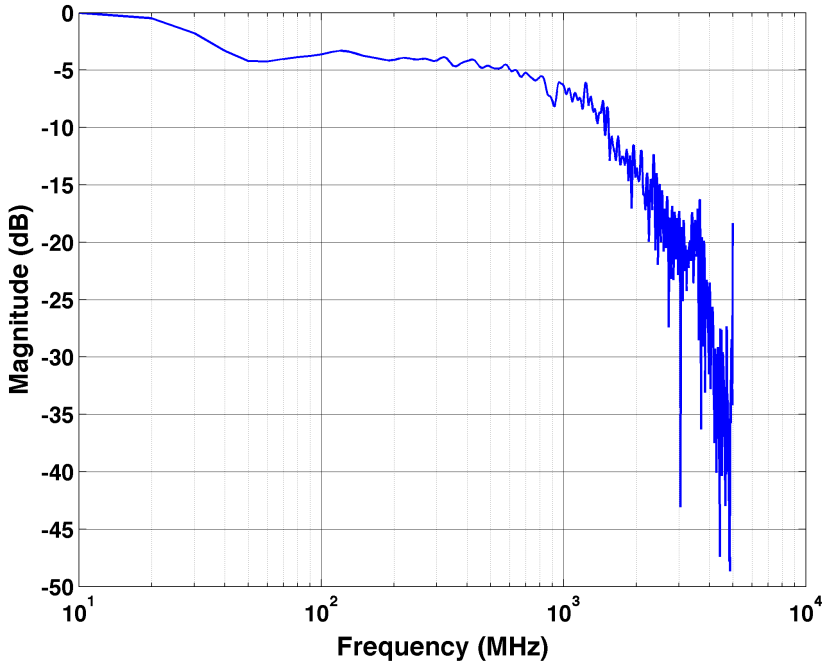


**Figure 2.18:** Estimated frequency response using the FFT built-in Matlab function. It indicates a slow response and fast response component with respective bandwidths of 40 MHz and 1 GHz.

# References


[1] G. P. Agrawal, *Fiber-Optic Communication Systems,* 4th ed., Hoboken, NJ: John Wiley & Sons, Inc., 2010.

[2] M. Legre, R. Thew, H. Zbinden, and N. Gisin, "High resolution optical time domain reflectometer based on 1.55μm up-conversion photon-counting module," *Optics Express,* vol. 15, no. 13, pp. 8237-8242, 2007. [Online]. Available: https://www.osapublishing.org/oe/abstract.cfm?uri=oe-15-13-8237

[3] D. Derickson, *Fiber Optic Test and Measurement,* Upper Saddle River, NJ: Prentice Hall – PTR, 1998.

[4] "Sampling Oscilloscope," 1989, Tektronix, Inc., [Online]. Available: http://www.cbtricks.com/miscellaneous/tech_publications/scope/sampling.pdf

[5] D. M. Pataca, P. Gunning, M. L. Rocha, J. K . Lucek, R. Kashyap, K. Smith, D. G. Moodie, R. P. Davey, R. F. Souza, and A. S. Siddiqui, "Gain-Switched DFB Lasers," *Journal of Microwaves and Optoelectronics,* vol. 1, no. 1, pp. 46-63, May 1997. [Online]. Available: http://www.google.com/url?sa=t&rct=j&q=&esrc=s&source=web&cd=8&ved=0CFkQFjAH&url=http%3A%2F%2Fwww.jmoe.org%2Fdownload.hp%3Ffile%3D12937338860.pdf%26nome%3DVolume%25201%2520%2520Number%25201%2520-%2520Gain-Switched%2520DFB%2520Lasers.pdf&ei=ygVbVai3JojboASXv4OQCg&usg=AFQjCNEW1tnFAUeMNlVLqdpOXA9bEUB-eg&sig2=N6ohb-EIM5RqIOVEGYuRpg&bvm=bv.93756505,bs.1,d.cGU

[6] NEC Laboratories America, Inc., "NEC's Φ50 μm InGaAs PIN-PD Coaxial Module for 2.5 Gb/s Fiberoptic Communications,"NR7500 Series datasheet, May 2002. [Online]. Available: http://www.cel.com/pdf/datasheets/nr7500bp.pdf

[7] Mitsubishi, "1.55 μm DFB-LD Module with Polarization Maintaining Fiber Pigtail," FU-68PDF-V510MxxB datasheet. [Online]. Available: http://pdf1.alldatasheet.com/datasheet-pdf/view/634/MITSUBISHI/FU-68PDF-V510MXXB.html

[8] Hittite Microwave Corporation, " MZ Optical Modulator Driver, DC-20 GHz," HMC870LC5 datasheet, v.05.0614. [Online]. Available: https://www.hittite.com/content/documents/data_sheet/hmc870lc5.pdf

[9] Silicon Labs, "Mixed Signal ISP Flash MCU Family," C8051F50x/F51x datasheet, rev. 1.2, 2011. [Online]. Available: https://www.silabs.com/Support%20Documents/TechnicalDocs/C8051F50x-51x.pdf

[10] Fiber Instrument Sales, Inc., "FIS Dual Window 1310/1550nm 2x2 Coupler 50/50 Split 250μm," [Online]. Available: http://www.fiberinstrumentsales.com

# Chapter 3

# OTDR Performance

There are a number of parameters used to describe the performance of an OTDR. The limit to each of parameters depends on instrumental characteristics, such as the transmitter pulse energy and noise in the receiver. This chapter analyzes three key performance characteristics of the ASIC-based OTDR, and discusses their tradeoffs. First, the two-point spatial resolution of the OTDR is tested. Then, the noise of the receiver is measured and its effect on accurately interpreting a signal is examined. Lastly, the noise is quantified in terms of the receiver sensitivity. The last section in this chapter discusses possible methods of improvement.

## 3.1 Spatial Resolution

Spatial resolution is the ability to measure two closely spaced events in a fiber, and is directly related to the pulse width and the receiver's sampling resolution. The minimum distance that can exist between two discrete events is approximately equal to the full-width half-maximum (FWHM) of the pulse. The shortest pulse that can be resolved by the receiver is determined by the receiver's bandwidth and its signal-sampling rate. For example, if the

200 pS transmitted pulse is preserved up until the detector, and the receiver has sufficient bandwidth, the OTDR ASIC can theoretically achieve a spatial resolution of 2 cm (Section 2.1). In this section, the spatial resolution of the ASIC-based OTDR from Chapter 2 is tested.

The experimental setup is shown in Figure 3.1. Two single mode fiber patch cables of different lengths are attached to the optical beam splitter, one on each end. The difference in fiber cable length, ΔL, varies from 1 to 30 cm. When an optical pulse is launched into the splitter, a Fresnel reflection occurs at both ends, but at different points in time. The two reflected light signals are coherent and therefore, their fields add constructively [9]. The resulting signal is a superposition of the two reflections.

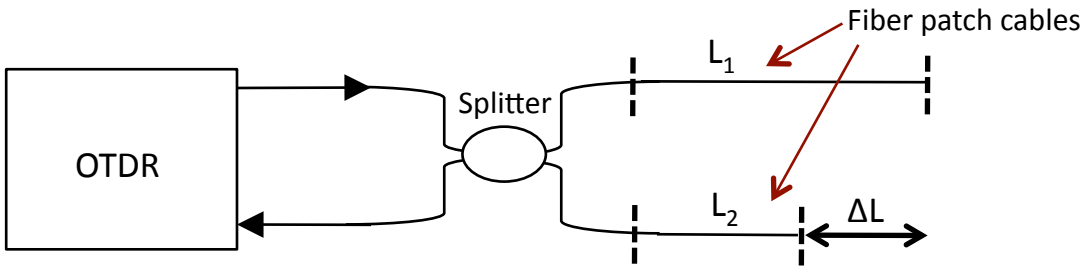


**Figure 3.1:** Experimental setup for testing two-point measurement resolution of OTDR ASIC.

Figure 3.2 shows the results from measuring two discrete events that are spaced 30 cm, 6 cm, 4 cm, 3 cm, and 1 cm apart. The two reflection peaks are distinguishable down to 3 cm spacing, and thus the achievable spatial resolution is 3 cm. The fact that 2 cm spatial resolution was not reached can be attributed to the limited receiver bandwidth, (Section 2.3). The pulse width at the output of the receiver is 300 pS, which is consistent with the FWHM-spatial resolution approximation.

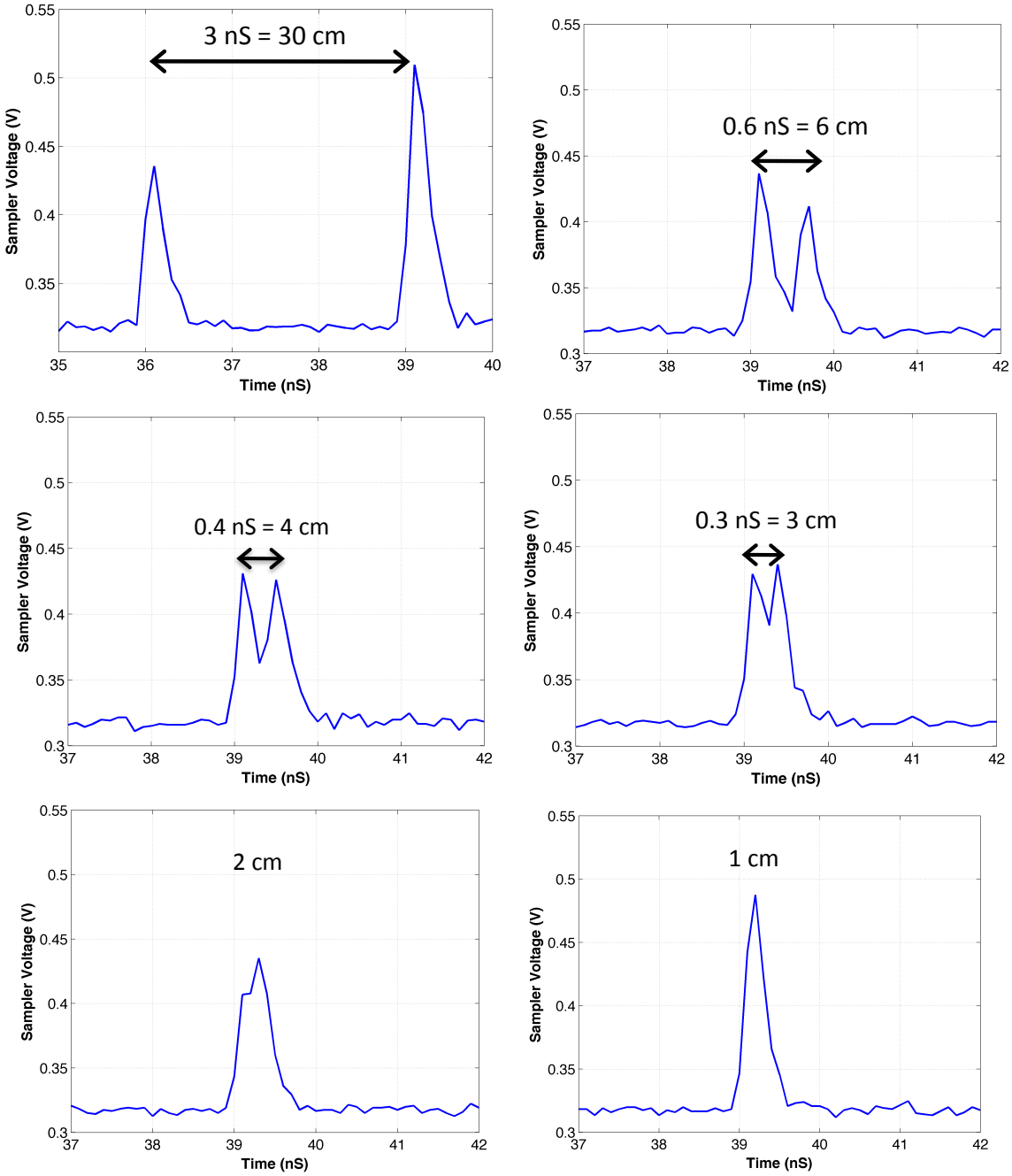


**Figure 3.2:** OTDR measurements of reflection from two separate fiber patch cables differ in lengths of 1-30 cm.

Using the frequency response derived in Section 2.3, it is possible to predict the spatial resolution for any given input pulse width. This was done in Matlab by simulating an ideal

pulse[10], and then filtering the signal with the receiver's transfer function from Figure 2.18. The resulting pulse width gave an estimate for the attainable spatial resolution.

The filtering was done with basic Fourier transform analysis. Figure 3.3 shows two example input signals, $x(t)$, and their corresponding filtered output signals, $y(t)$. The input and output signals of either case are related through convolution as shown in Eq. 3.1, where $h(t)$ is the impulse response of the receiver [10]. Using the convolution property, Eq. 3.1 can be expressed in terms of the Fourier transform of the signals (Eq. 3.2). Then, the receiver's response to an input signal is the inverse Fourier transform[11] of the product $H(j\omega)X(j\omega)$ (Eq. 3.3). Appendix C shows a basic Matlab script for performing these functions to filter data.

(Convolution) $$y(t) = h(t) * x(t) \tag{3.1}$$

$$Y(j\omega) = H(j\omega)X(j\omega) \tag{3.2}$$

(Inverse Fourier transform) $$y(t) = \mathcal{F}^{-1}\left\{H(j\omega)X(j\omega)\right\} \tag{3.3}$$

[10] The RECTPULS built-in Matlab function was used to simulate an ideal pulse. RECTPULS(T,W) generates samples of a continuous, aperiodic rectangle with unity-height and width, W. The generated samples correspond to the points specified in the array, T. In this specific experiment, T was incremented by 0.1 nS, which is the sampling rate of the ASIC receiving [19].

[11] IFFT is the built-in Matlab function used to perform the inverse discrete Fourier transform [20].

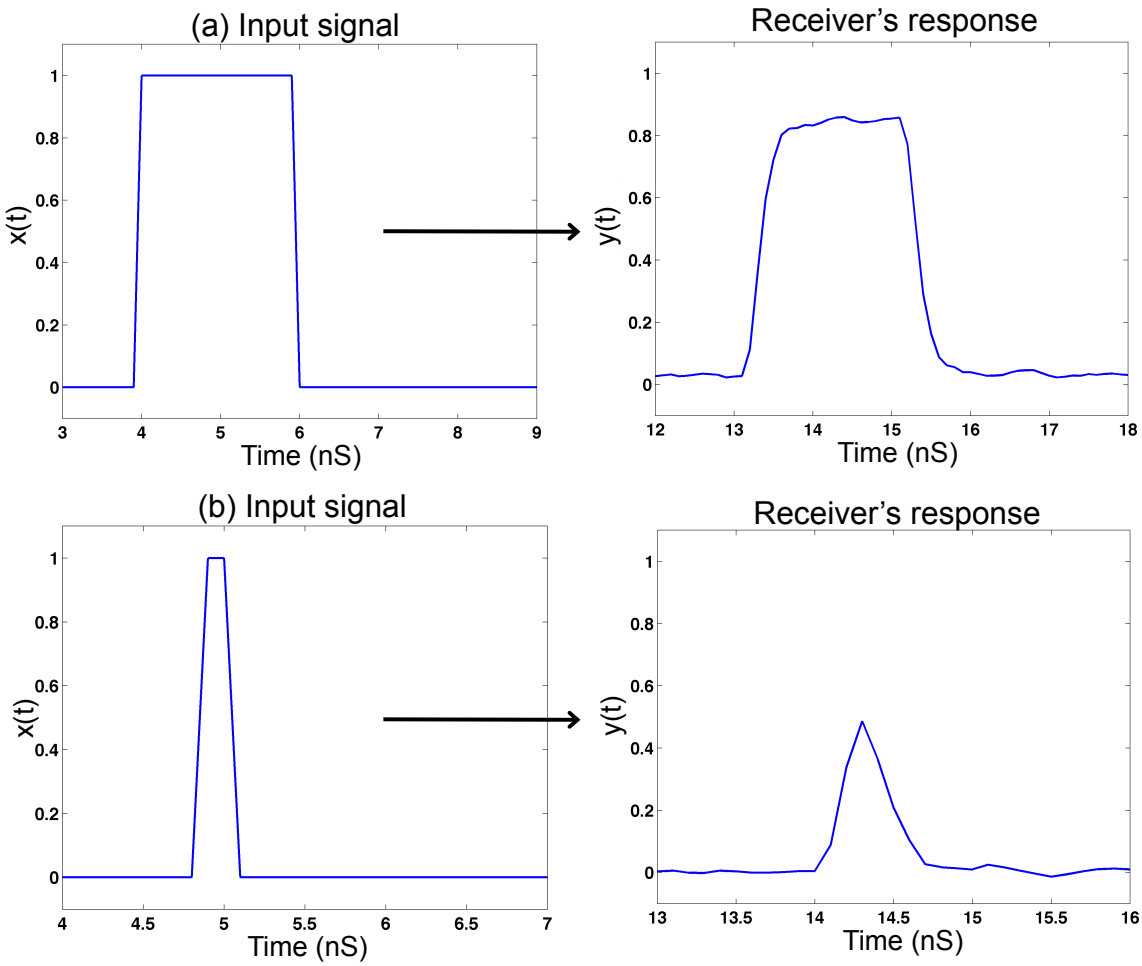


**Figure 3.3:** Simulated ideal input pulse and its corresponding output response when filtered with the receiver's impulse response. (a) Input pulse width: 2 nS, output pulse width: 2 nS. (b) Input pulse FWHM: 200 pS, output pulse FWHM: 320 pS.

Figure 3.4 plots the two-point spatial resolution for input pulse widths of 100 pS to 1.5 nS. Initially, the slope curves because short pulse widths are broadened when passed through the receiver, and the resolution is degraded. When the input pulse bandwidth meets the receiver's bandwidth, the pulse width is preserved. This is seen in the linear trend region, where the spatial resolution is equal to the input pulse width.

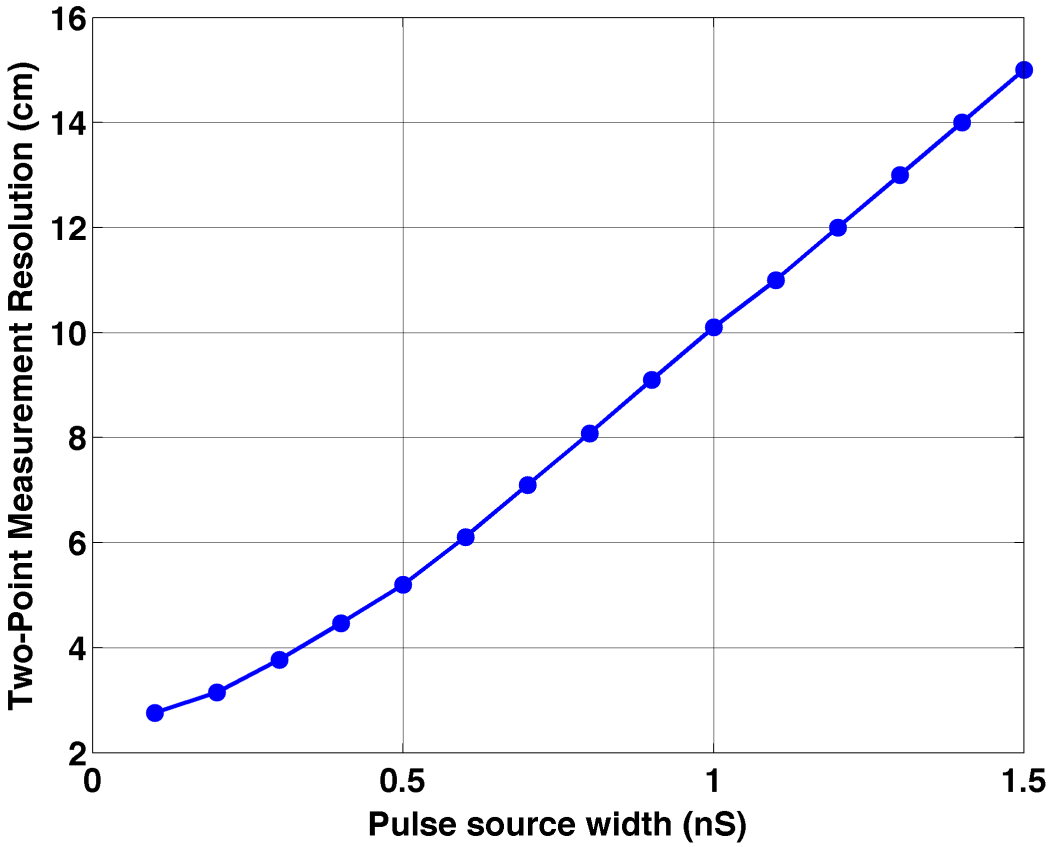


**Figure 3.4:** Spatial resolution for a given input pulse width

## 3.2 Noise Analysis

Noise is broadly defined as any signal present in the receiver other than the signal of interest. The amount of noise present ultimately determines the quality of the desired signal and the sensitivity of the receiver. Therefore, an understanding of the sources of noise is crucial in characterizing a receiver's performance.

The two primary noise mechanisms are thermal noise and shot noise [1,2,5]. Thermal noise is governed by the random motion of charge carriers due to the non-zero temperature of a conductive material. The extent to which the charge carriers move is a direct function of temperature, and is present regardless of the signal. As the temperature increases, the

agitation of charge carriers increases, and hence the thermal noise level. Shot noise arises from the fact that electric current is composed of discrete carriers, which form an average current flow. When individual carriers cross a potential barrier, they do so randomly, and noise is generated. Shot noise is dependent on any current flow in the receiver, including the generated photocurrent and the reverse leakage current in the photodiode. In most practical settings, however, the shot noise is relatively small and can be neglected [1,4]. This is a good assumption for the OTDR application since the average optical power level is very low. Thermal noise is then the dominant source of noise in the receiver's circuit.

The signal that is sampled at the output of the receiver can be modeled as the intended signal s(t), plus the total noise, n(t) (Figure 3.5). The noise exhibits Gaussian statistics [1] and thus can be modeled as a stationary Gaussian random process with zero mean, $\mu$ and some variance, $\sigma^2$.

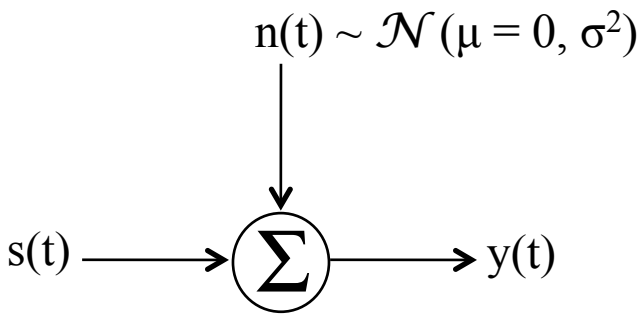


**Figure 3.5:** Conceptual model for the signal, y(t), at the output of the ASIC receiver

To measure the noise statistics, several thousand voltage samples were taken at the receiver with no optical signal incident on the photodiode. Figure 3.6 shows an example measurement. Since there is no signal component in this measurement, what is captured is

the DC offset of the instrumentation amplifier in the receiver[12] plus additional noise. Figure 3.7 shows the distribution of samples is well approximated as a Gaussian random process. From the noise distribution, an estimate of the noise variance $\sigma^2$, and the root-mean-square (RMS) noise level $\sigma_{rms}$, can be found [1]. For approximately 10,000 samples with no averaging[13], the variance and RMS noise level are 0.00278 $V^2$ and 52.8 mV respectively. The sample mean is 314.2 mV, which is consistent with the lowest offset setting of the receiver. Note, that this is the noise measured at the output of the receiver. The input-referred noise can be found by dividing the RMS noise level by gain of the receiver [5], as shown in Eq. 3.4.

(Input-referred noise power)

$$\left\langle i_n \right\rangle = \frac{0.0528\ \text{V}}{22989\ \text{V/A}} = 2.297\ \mu\text{A}_{rms} \qquad (3.4)$$

$$\left\langle i_n^2 \right\rangle = 5.275 \times 10^{-12}\ \text{A}^2$$

[12] The instrumentation amplifier, which internal to the OTDR ASIC, has adjustable gain and offset. For more information on these settings, see Section 2.6.1.

[13] The OTDR ASIC can be programmed to average several sample measurements. Section 2.1 outlines the sequence of software functions that the ASIC performs during an OTDR measurement.

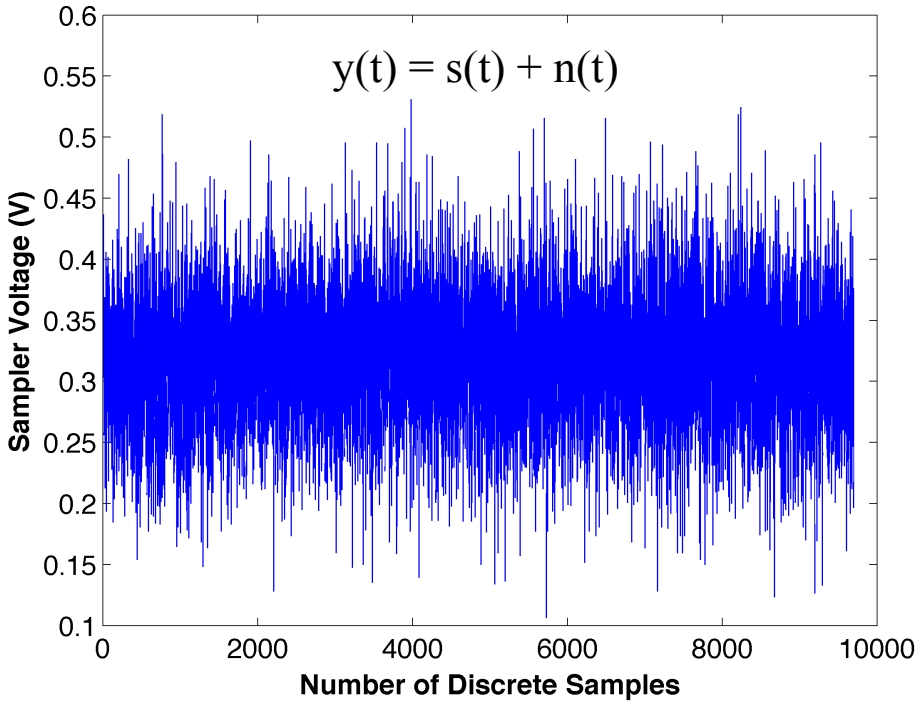


**Figure 3.6:** Measured signal with noise at the output of the ASIC receiver, where s(t) is the DC offset and n(t) is random noise.

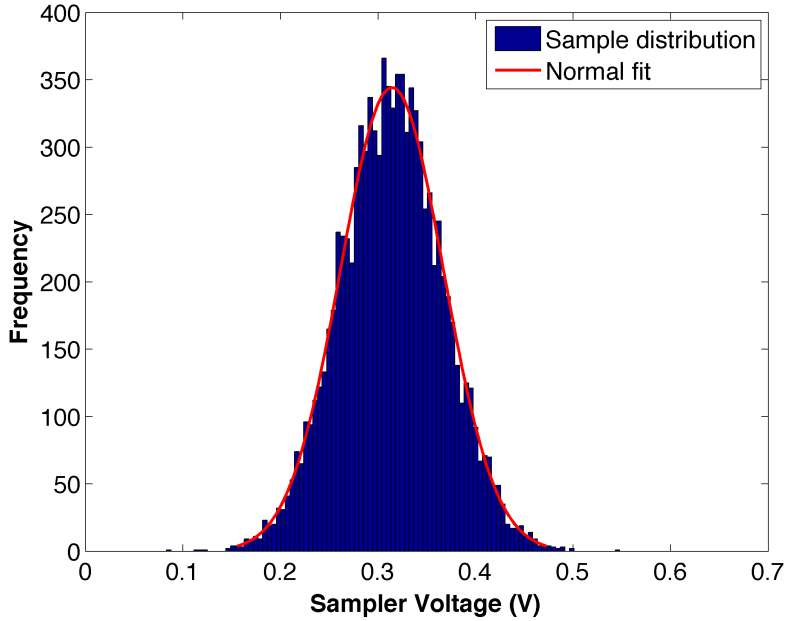


**Figure 3.7:** Sample noise distribution. Number of samples = 9,701; $\sigma_{rms}$ = 52.8 mV; $\mu$ = 314.2 mV

Thermal noise is random by nature, which means the instantaneous value of noise cannot be predicted, and therefore, noise-cancelling techniques are ineffective. On the other hand, signal averaging can reduce the effects of noise. Assuming the noise has zero mean, the noise randomness will add destructively, and the RMS noise level (standard deviation) will tend to zero.

The reduction of noise by means of averaging can be described through statistical analysis. Let $X[k]$ be a sample of the signal with a variance $\sigma_x^2$, such as the one in Figure 3.6. If we repeat this measurement $N$ times and average the signal strength at each finite sampling point $i$, then $Y[k]$ is equal to the sample mean (Eq. 3.5). In the expression below, the index $i$ represents the discrete values collected at each time instance during data acquisition. The variance of Y[k] is then defined by Eq 3.6. Therefore, the standard deviation decreases with signal averaging by a factor of $\sqrt{N}$, where $N$ is the number of averages (Eq. 3.7).

(Sample mean)
$$Y[k] = \frac{1}{N}\sum_{i=1}^{N} X_i[k] \tag{3.5}$$

$$\begin{aligned}\sigma_y^2 &= Var\left(\frac{1}{N}\sum_{i=1}^{N} X_i[k]\right)\\ &= \frac{1}{N^2}\left(\sum_{i=1}^{N}\sigma_x^2\right)\\ &= \frac{N\cdot\sigma_x^2}{N^2}\\ &= \frac{\sigma_x^2}{N}\end{aligned}$$

(Sample variance) (3.6)

(Sample standard deviation)
$$\sigma_y = \frac{\sigma_x}{\sqrt{N}} \tag{3.7}$$

Figure 3.8 shows the reduction of RMS noise level with averaging. The noise level can be reduced to 0.8969 mV with 10,000 averages. The leveling off that occurs around 5,000 averages ($\sigma_{rms}$ ~ 1 mV) can be attributed to the deviation from Gaussian. Hence, the reduction in RMS noise level no longer follows Eq. 3.7.

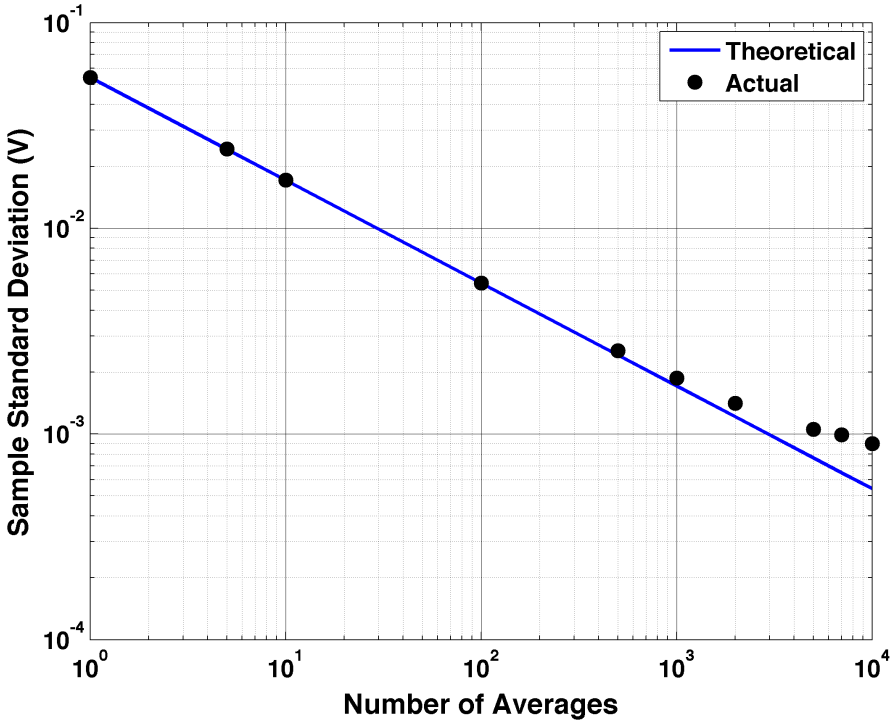


**Figure 3.8:** Reduction of noise with signal averaging.

A well-known characteristic used to quantify the quality of a measurement is the signal-to-noise ratio (SNR), given by the ratio of the average signal power over the average noise power [1-3].

(Signal-to-noise ratio)
$$SNR = \frac{\left\langle i_{signal}^2 \right\rangle}{\sigma^2} \tag{3.8}$$

The signal-to-noise ratio at the output of the OTDR receiver was calculated from the following definition:

$$SNR = \left( \frac{A_{signal}}{\sigma_{rms}} \right)^2 \tag{3.9}$$

$$SNR_{dB} = 20\log\left( \frac{A_{signal}}{\sigma_{rms}} \right)$$

$A_{signal}$ represents the peak amplitude of the trace and $\sigma_{rms}$ represents the RMS noise voltage (standard deviation), which is obtained from a part of the trace where no reflections are present. Figure 3.9 illustrates the SNR calculation. It can be seen by Eq. 3.8, that the SNR will improve with averaging as the RMS noise level decreases. Figure 3.10 plots the improvement of SNR with averaging. The maximum SNR achieved (relative to the OTDR reflection peak in Figure 2.13) is 49 dB with 10,000 averages; that is 35.62 dB higher than the case with no averaging.

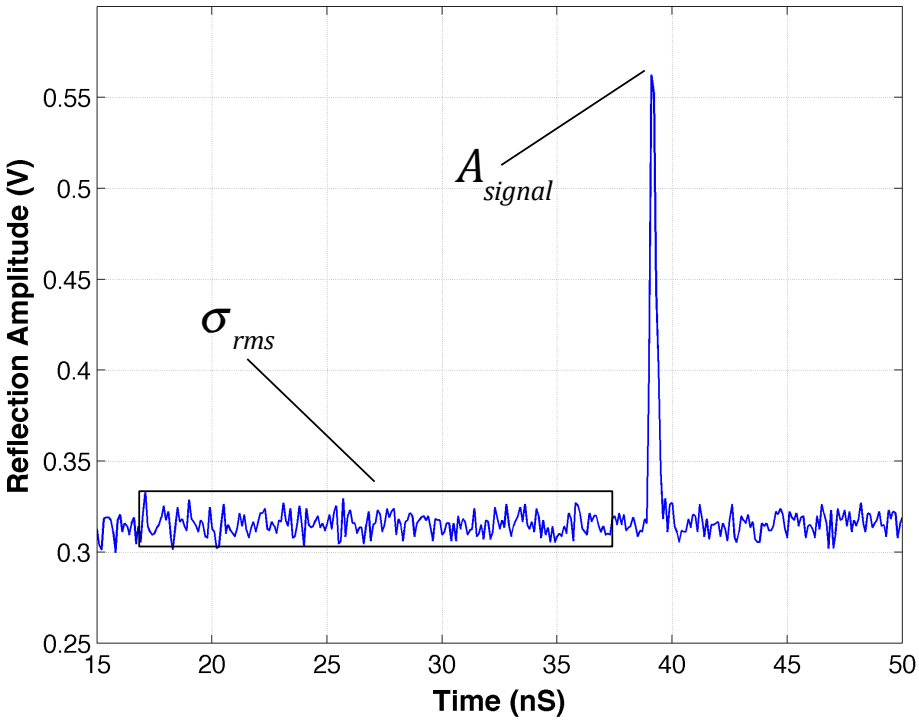


**Figure 3.9:** Illustration of SNR calculation for an OTDR measurement

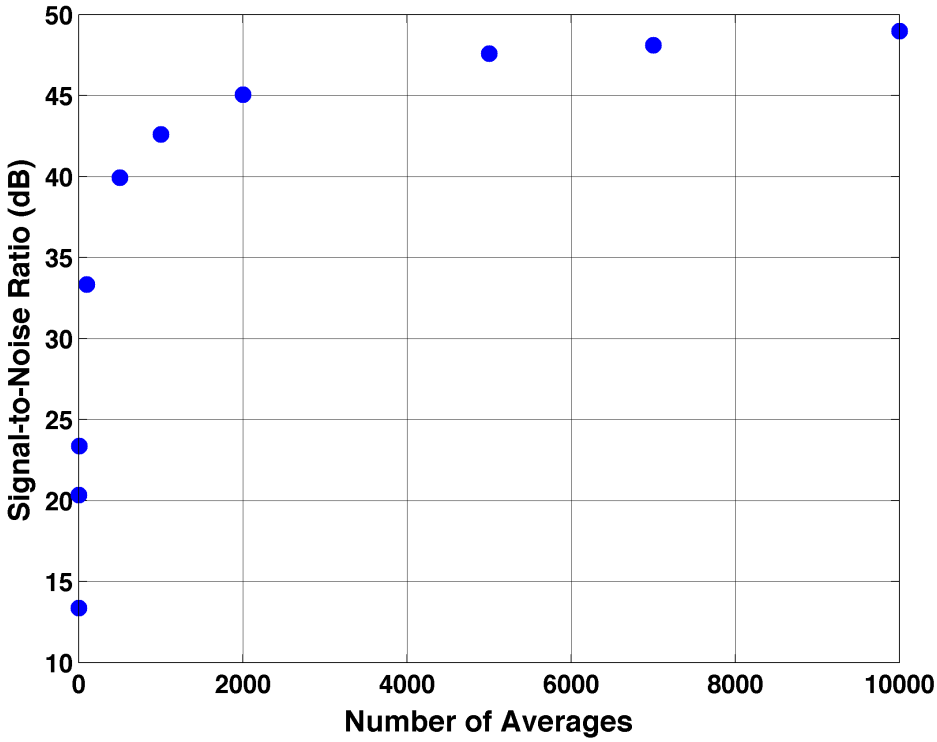


**Figure 3.10:** SNR improvement with signal averaging. Note that this is specific to the OTDR measurement in Figure 2.13, which has a signal amplitude of 252.3 mV. The SNR improved by 35.62 dB with 10,000 averages.

## 3.3 Sensitivity

The sensitivity of a receiver is defined as the weakest optical signal that can be detected with an acceptable quality [2,8]. As light travels down a fiber, it experiences loss due to Rayleigh scattering, fusion splices, mechanical connectors, and faults along the fiber. The signal power must be at or above the noise floor by the time it reaches the detector in order to be interpreted accurately. The pulse width affects the receiver' s amplification of the input signal, and therefore, plays a role in determining the sensitivity. In this section, first a definition of the noise floor is established. Then, the receiver's sensitivity is found for various pulse source widths and number of averages.

The noise floor can be defined as the noise mean fluctuation, or standard deviation, $\sigma_{rms}$, which was in found in Section 3.2 to be 52.8 mV with no averaging. This is equivalent to having a signal-to-noise ratio of 1, in which case the signal of interest is smaller than the peak-to-peak noise variation, and therefore, may not be recovered. Another common definition of noise floor is the "98% noise level," where the boundary is positioned below 2% of the noise fluctuation. Figure 3.11 illustrates the 98% noise level. For a Gaussian distribution of noise, this level occurs at roughly $2.05 \cdot \sigma_{rms}$ [8]. Although this definition of noise floor reduces the OTDR measurement range, it is more practical.

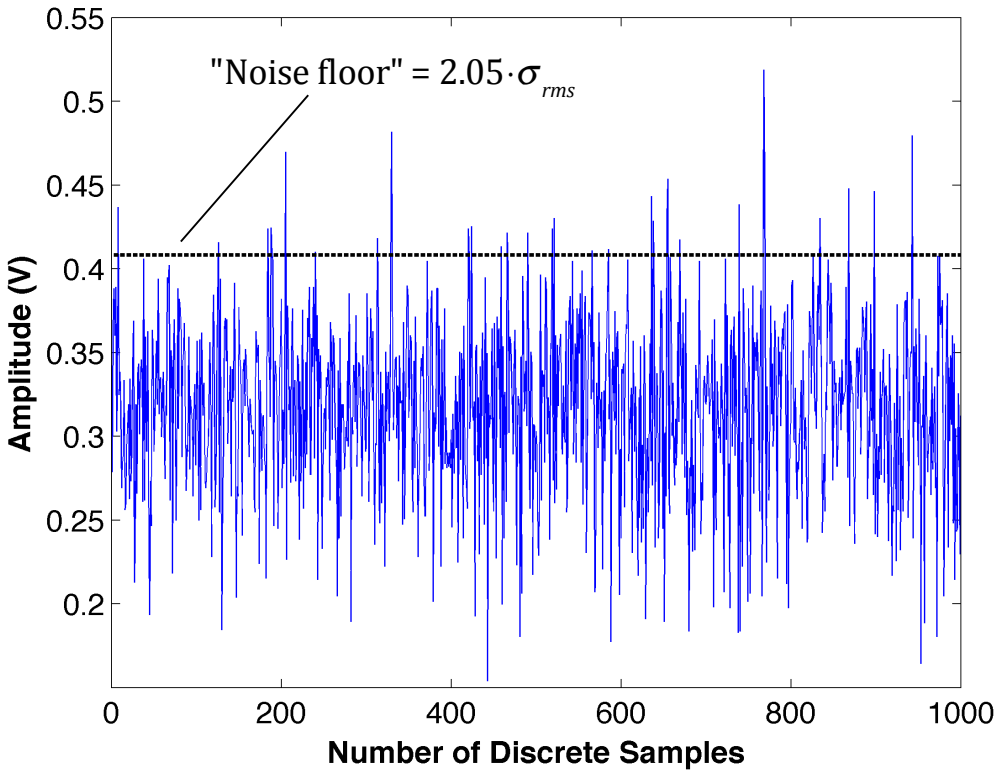


**Figure 3.11:** Illustration of 98% noise level.

The noise floor is measured at the output of the ASIC receiver. Then, to find the minimum detectable optical power, it is divided by the effective gain of the receiver, which

varies with the input pulse width due to bandwidth limitations. As seen in the receiver's frequency response (Figure 2.18), for high input pulse bandwidths (or short pulse widths), the gain is reduced. As a result, the receiver's sensitivity degrades. This phenomenon was simulated in Matlab[14] by filtering pulses of various widths and finding their pulse conversion gain. The total gain for a given input pulse is then the pulse conversion gain multiplied by the DC gain, which is 20,805 V/W. Figure 3.12 shows two example input pulses and the corresponding filtered outputs. The 2 nS wide pulse has a pulse gain conversion of 0.858, which results in a total gain of $\left(0.858\right)\left(20{,}805\ \mathrm{V/W}\right)=17{,}851\ \mathrm{V/W}$. While the 200 pS wide pulse has a total gain of only $10{,}120\ \mathrm{V/W}$. Figure 3.13 plots the resulting sensitivity as a function of pulse source width and number of averages. The sensitivity begins to level out around 0.8 nS because the input pulse bandwidth is within the flat gain region of the receiver's frequency response. The highest achievable sensitivity of the receiver is -39.88 dBm with a pulse width of 2 nS and 10,000 averages; however, it is not a huge improvement from -39.68 dBm, which is achieved with a 0.8 nS pulse width. Increasing the pulse width enables high sensitivity and enhances the OTDR's measurement range; however, it also degrades the two-point spatial resolution as shown in Section 3.1. Hence, there is a trade-off between sensitivity and spatial resolution.

[14] This is the same filtering experiment done in Section 3.1. Previously, only the resulting pulse width for a given input pulse width was considered. In this section, the normalized gain for a given input pulse width is examined.

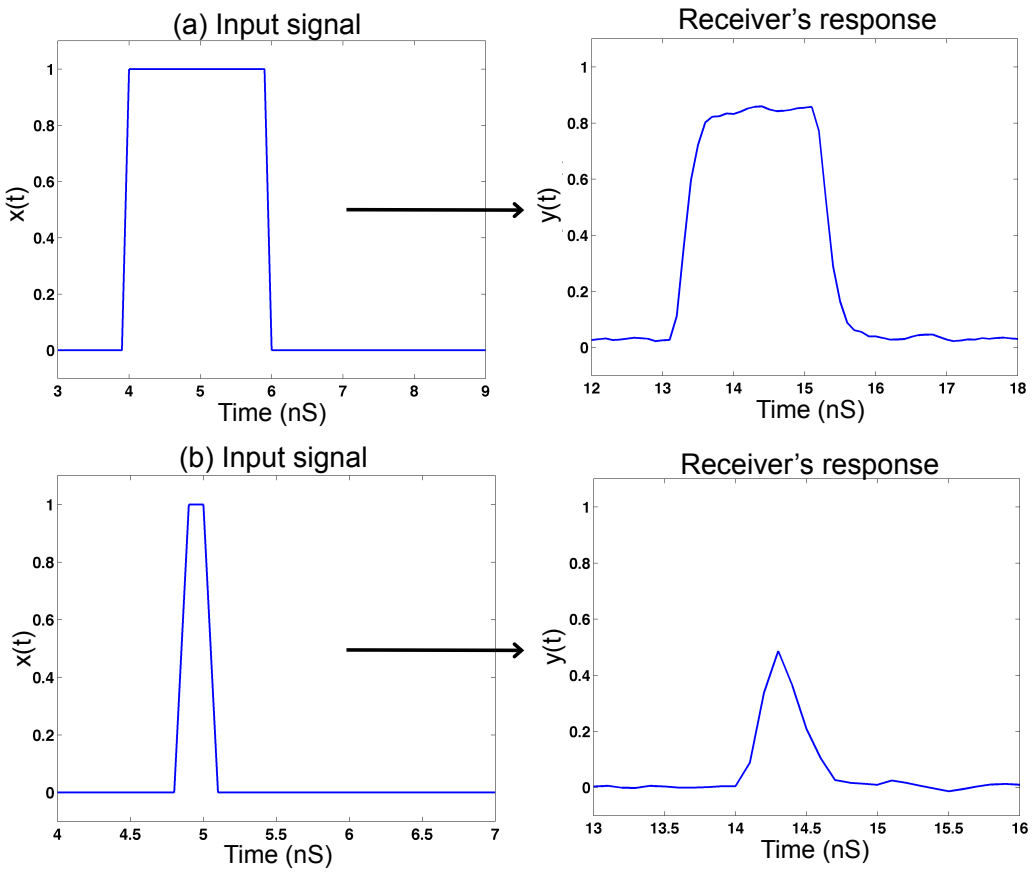


**Figure 3.12:** Simulated ideal input pulse and its corresponding output response when filtered with the receiver's impulse response. (a) Pulse conversion gain: 0.858 (b) Pulse conversion gain: 0.4864

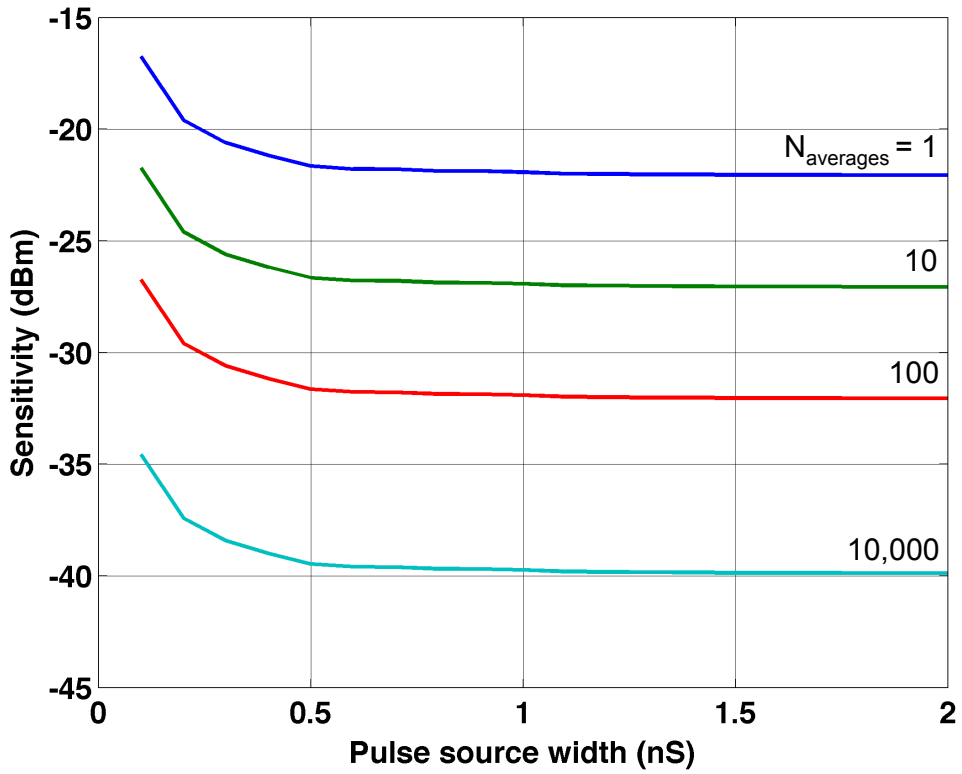


**Figure 3.13:** OTDR receiver sensitivity as a function of input pulse width and number of averages ($N_{averages}$).

## 3.4 Methods of Improvement

The performance capabilities and constraints of the ASIC-based OTDR were examined in Sections 3.1-3.3. The bandwidth of the receiver was seen to be a limiting factor to the spatial resolution. Furthermore, signal averaging reduced the effects of thermal noise in the receiver; however, that seemed to have its own limitation as well. This section touches on a few techniques for improving spatial resolution and sensitivity.

Reducing the pulse width and/or increasing the signal receiving bandwidth can improve the spatial resolution. One way to increase the bandwidth is by minimizing parasitic components as much as possible. For instance, the PIN photodiode used the OTDR comes in a coaxial package, which has been known to contain a lot of stray capacitance [11-12].

Replacing this packaged photodiode with a bare die would help eliminate parasitics associated with component packaging.

Alternatively, the spatial resolution can be improved through deconvolution processing techniques. The principle of a deconvolution algorithm goes back to the representation of two signals as a convolution (Eq. 3.10), which becomes a product in the frequency domain (Eq. 3.11). This concept was visited in Section 3.1. The input signal is then recovered by dividing the output in the frequency domain by the transfer function of the receiver, and taking the inverse Fourier transform (Eq. 3.13). If the OTDR system is assumed to be a linear time-invariant (LTI) system, then essentially any input can be recovered from the observed output and the impulse response of the receiver. In a real OTDR system, however, the restoration of the input signal is more complicated than this because the measured signal is superimposed by noise. Various deconvolution techniques that address this issue have been proposed [13-14].

(Convolution) $$y(t) = h(t) * x(t) \tag{3.10}$$

(Frequency domain representation) $$Y(f) = H(f)X(f) \tag{3.11}$$

$$X(f) = \frac{Y(f)}{H(f)} \tag{3.12}$$

(Inverse Fourier transform) $$x(t) = \mathcal{F}^{-1}\left\{X(f)\right\} \tag{3.13}$$

To enhance the sensitivity of the receiver, a photodetector with high gain, such as an Avalanche Photodiode (APD), can be used. An APD is known for its high sensitivity because one electron can result in an "avalanche" of electrons, all of which contribute to the generated photocurrent [15]. The generated photocurrent strongly depends on the electric field within the diode, and therefore, on the reverse bias, $V_r$. Eq. 3.12 shows the avalanche

multiplication factor, where $V_{br}$ is the breakdown voltage and $n$ is a temperature dependent constant.

(Avalanche multiplication factor)
$$M = \frac{1}{1 - \left( \frac{V_r}{V_{br}} \right)^n} \tag{3.12}$$

When the APD is biased above its breakdown voltage, it is said to be operating in Geiger mode [29]. Geiger mode APDs have gain on the order of $10^6$, which is sufficient to detect a single photon, and thus makes them even more sensitive than linear APDs. In contrast to linear APDs, however, the detection of a signal is binary. When an avalanche occurs and the current surpasses a threshold, the detection is counted as one regardless of how many photons induced the avalanche – its either present or not. There is a probability, however, that the photon(s) may not be detected. Raising the bias voltage increases the probability of detection, but also increases the dark count rate, which is the rate of falsely detected signals due to thermal excitation or tunneling. A lot of effort has been put into the design of photon counting OTDRs with a Geiger mode APD in order to enhance sensitivity, resolution, and measurement accuracy [16-18].

As an alternative to choosing a high gain photodiode, an optical amplifier can be used to boost the weak signal just before the detector. Both APDs and optical amplifiers can provide extraordinary gain, but they also introduce a source of noise. Chapter 4 explores the use of a semiconductor optical amplifier as a preamplifier.

# References


[1] G. P. Agrawal, *Fiber-Optic Communication Systems,* 4th ed., Hoboken, NJ: John Wiley & Sons, Inc., 2010.

[2] D. Adamy, *Practical Communication Theory,* 2nd ed. Edison, NJ: SciTech Publishing, 2014, pp 15-21 and 93-108.

[3] S. B. Alexander, *Optical Communication Receiver Design,* Bellingham, WA: The Society of Photo-Optical Instrumentation Engineers, 1997. [Online]. Available: http://ebooks.spiedigitallibrary.org.proxy.library.ucsb.edu:2048/book.aspx?bookid=196

[4] N. Kobayashi, R. Furukawa, Y. Ozeki, T. Ushikubo, and M. Akiyama, "A Low Noise and Broad-Band Optical Receiver for 10 Gb/s Communication Systems," *Gallium Arsenide Integrated Circuit (GaAs IC) Symposium, 1992. Technical Digest 1992, 14th Annual IEEE,* pp. 287-290, Oct. 1992. [Online]. Available: http://ieeexplore.ieee.org /stamp/stamp.jsp?tp=&arnumber=247275

[5] B. Razavi, *RF Microelectronics,* 2nd ed., Upper Saddle River, NJ: Pearson Education, Inc., 2012, pp. 7-60.

[6] C. M. Benta, L. Baudzus, and P. M. Krummrich, "Signal to Noise (SNR) Enhancement Comparison of Impulse-, Coding, and Novel Linear-Frequency-Chirp-Based Optical Time Domain (OTDR) for Passive Optical Network (PON) Monitoring Based on Unique Combinations of Wavelength Selective Mirrors," *Photonics,* 1, pp. 47-66, March 2014. [Online]. Available: http://www.mdpi.com/2304-6732/1/1/33

[7] H. Geiger and J. P. Dakin, "Low-Cost High-Resolution Time-Domain Reflectometry for Monitoring the Range of Reflective Points," *Journal of Lightwave Technology,* vol. 13, no. 7, pp. 1282-1288, Jul. 1995. [Online]. Available: http://ieeexplore.ieee.org/stamp/ stamp.jsp?arnumber=400686

[8] D. R. Anderson, L. Johnson, and F. G. Bell, *Troubleshooting Optical-fiber Networks,* 2nd ed. San Diego, CA: Elsevier Academic Press, 2004.

[9] L. A. Coldren, S. W. Corzine, and M. L. Masanovic, *Diode Laser and Photonic Integrated Circuits,* 2nd ed., Hoboken, NJ: John Wiley & Sons, Inc. 2012.

[10] A. V. Oppenheim, A. S. Willsky, and S. H. Nawab, *Signals and Systems,* 2nd ed. Upper Saddle River, NJ: Pearson Education, 1997.

[11] G. J. Cleary, A. M. Moloney, and A. P. Marrison, "Investigating the Effects of Package Capacitance on the Frequency Response of Shallow Junction Avalanche Photodiodes," *Proc. Of SPIE,* vol 6124, Mar. 2006. [Online]. Available: http://proceedings.spiedigital library.org/proceeding.aspx?articleid=1275291

[12] S. J. Zhang, N. H. Zhu, Y. Liu, and L. Xie, "Potential frequency bandwidth estimation of TO packaging techniques for photodiode modules," *Optical & Quantum Electronics,* vol. 38, iss. 8, pp, 675-682, Aug. 2006. [Online]. Available: http://connection.ebscohost.com/c/articles/22911618/potential-frequency-bandwidth-estimation-packaging-techniques-photodiode-modules

[13] F. Maasoumi and A. Bahrampour, "Employing the ForWARD Method to Improve Resolution of Conventional OTDR for Application in SHM," *Journal of Electronic Science and Technology,* vol. 8, no. 1, pp. 69-73, Mark 2010. [Online]. Available: http://www.journal.uestc.edu.cn/archives/2010/1/8/69-7321611.pdf

[14] S. Mohr, "Characterization of plastic optical fiber by optical time-domain reflectometry," *Proc. Of SPIE,* vol. 1799, Feb. 1993. [Online]. Available: http://proceedings.spiedigital library.org/proceeding.aspx?articleid=1001373

[15] S. O. Kasap, "Photodetectors" in *Optoelectronics and Photonics,* Upper Saddle River, NJ: Pearson Education, Inc., 2013, pp 230-234.

[16] P. Eraerds, M. Legre, J. Zhang, H. Zbinden, and N. Gisin, "Photon Counting OTDR: Advantages and Limitations," *Journal of Lightwave Technology,* vol. 28, no. 6, pp. 952-964, Mar. 2010. [Online]. Available: http://ieeexplore.ieee.org/stamp/stamp.jsp?arnumber=5371875

[17] F. Scholder, J. Gautier, M. Wegmuller, and N. Gisin, "Long-distance OTDR using photon counting and large detection dates at telecom wavelength," *Optics Communications,* vol. 213, pp. 57-6, Sept. 2002. [Online]. Available: http://www.unige.ch/gap/qtech/_media/ publications:bib:opt_comm_pc-otdr.pdf

[18] M. Wegmuller, F. Scholder, and N. Gisin, "Photon-counting OTDR for Local Birefringence and Fault Analysis in the Metro Environment," *Journal of Lightwave Technology,* vol. 22, no. 2, pp. 1-11, Feb. 2004. [Online]. Available: http://www.unige.ch/gap/quantum/_media/publications:bib:photdrme.pdf

[19] MathWorks, "Rectangular pulse shaping," [Online]. Available: http://www.Mathworks.com/help/comm/ref/rectpulse.html

[20] MathWorks, "Inverse fast Fourier transform," http://www.mathworks.com/help/matlab/ref/ifft.html

# Chapter 4

# The Use of a Semiconductor Optical Amplifier as a Preamplifier

A semiconductor optical amplifier (SOA) is essentially a laser without optical feedback. Anti-reflection (AR) coating is applied to the facets to prevent reflections and lasing. Optical amplification in an SOA is achieved through stimulated emission. As the gain region is electrically pumped with current, charge carriers accumulate in the conduction band. Then, when a photon enters the device, it perturbs the system causing electron-hole recombination and generation of an excess photon.

SOAs can potentially increase the sensitivity of a receiver by enhancing a low power signal prior to the photodiode. In addition, however, SOAs introduce noise through amplified spontaneous emission (ASE). This chapter explores the use of an SOA as a preamplifier to the OTDR receiver (Figure 4.1). The SOA that is investigated employs a hybrid waveguide structure in which III-V layers are bonded to a passive silicon waveguide. Preliminary measurements were done on the gain and noise characteristics of the SOA; however further research on the SOA-OTDR integration is necessary.

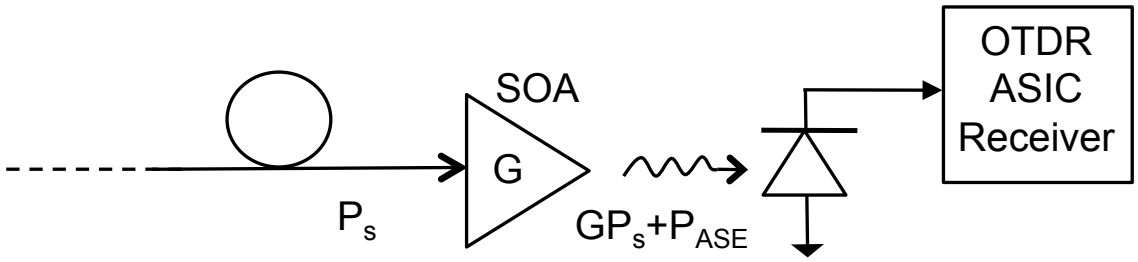


**Figure 4.1:** Theoretical schematic of optical preamplifier in OTDR scheme. The SOA amplifies the signal, but also adds ASE noise. The signal at the output of the SOA is then the amplified input power plus the ASE noise power.

## 4.1 The Hybrid Silicon SOA

The motivation for silicon photonics comes from the technological advances made in silicon processing, which have allowed for low-cost and high-volume manufacturing [10]. One outcome from the development of silicon photonics is the photonic-electronic integration on a single substrate. While this type of integration has several advantages [8-9], it still faces some challenges in dealing with the basic material properties of silicon [1]. Namely, that silicon has an indirect bandgap, which leads to dominantly non-radiative recombination over radiative recombination. As a result, the light generation efficiency is low. To overcome this problem in using silicon as an optical gain element, the hybrid silicon device platform has been proposed [2-3].

In the hybrid waveguide structure, III-V active layers are bonded to a passive silicon waveguide. The optical mode is confined by both the silicon and III-V waveguide, which allows for optical gain in the active layers and efficient light coupling to the passive waveguide. Varying the dimensions of the silicon waveguide (with fixed III-V dimensions) can control the amount of mode overlap in the III-V region. In general, decreasing the silicon waveguide width pushes the optical mode into the III-V region, which increases the quantum

well confinement and decreases the Si confinement [3]. The effects of confinement factor on gain characteristics are shown in Section 4.3.

## 4.2 Theory of SOA in OTDR Scheme

The fundamental principle of placing an SOA before the photodiode is that the gain of the optical receiver is enhanced by a factor of the SOA gain, $G$. In addition to amplifying the signal, the SOA adds optical noise due to amplified spontaneous emission (ASE), which manifests as current fluctuations in the receiver circuit. The electrical SNR at the photodetector then becomes

(Electrical SNR with optical amplifier)
$$SNR = \frac{\left\langle i_{signal}^2 \right\rangle}{\sigma^2} = \frac{R_d^2 \left(GP_s\right)^2}{\sigma_{ASE}^2 + \sigma_T^2} \tag{4.1}$$

where $\sigma_{ASE}^2$ is the ASE contribution to noise and $\sigma_T^2$ is the thermal noise in the receiver circuit. The shot noise term has been neglected since thermal noise exceeds shot noise in the OTDR application.

## 4.3 Experiment and Results

Figure 4.2 shows the device structure of the SOA used in the following experiments. The facets were AR-coated in order to reduce reflectivity. The III-V region consists of three quantum wells with 0.85% strain. These layers are bonded to a silicon passive waveguide, which is fabricated on a silicon-on-insulator (SOI) wafer. The silicon waveguide has a height of 500 nm; its width was varied among four devices from 0.95 to 1.6 μm.

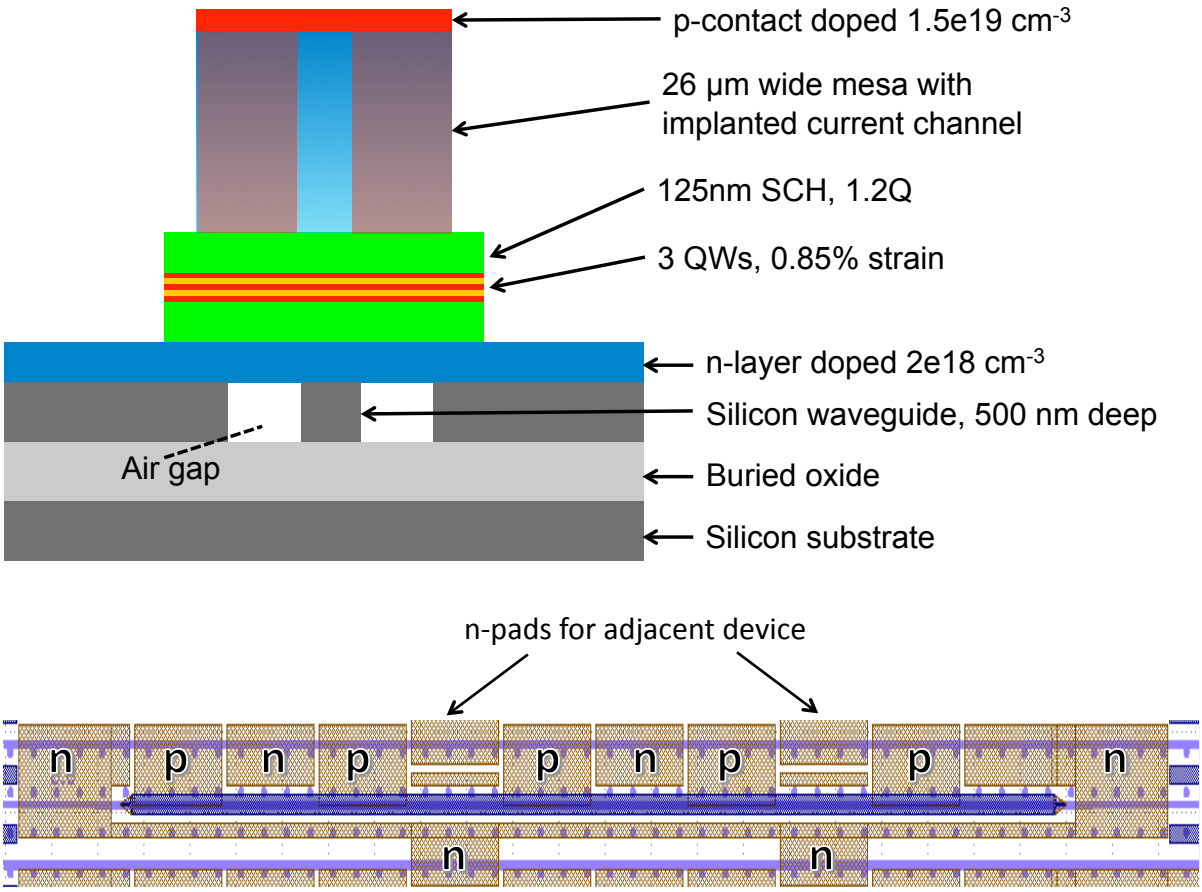


**Figure 4.2: (top)** Cross-sectional structure of hybrid silicon SOA **(bottom)** Top view of pad layout of SOA

During the experiment, the chip is mounted on a temperature controlled stage set to 20° C and current is injected through the p-contact. Figure 4.3 illustrates the experimental setup. Light in the C-band is launched and collected through lensed fibers at both the input and output facets of the chip. The input light source consists of a wavelength-tunable laser, erbium-doped fiber amplifier (EDFA), and a variable optical attenuator. The EDFA is needed to reach the SOA's gain saturation region. The input power is varied with the optical attenuator. A 3-paddle polarization controller is adjusted to maximize the TE polarized light.

Lastly, a 1 nm optical filter was placed at the output to eliminate out-of-band ASE noise. The system loss and facet loss were measured to be 11.75 dB and 9 dB respectively.

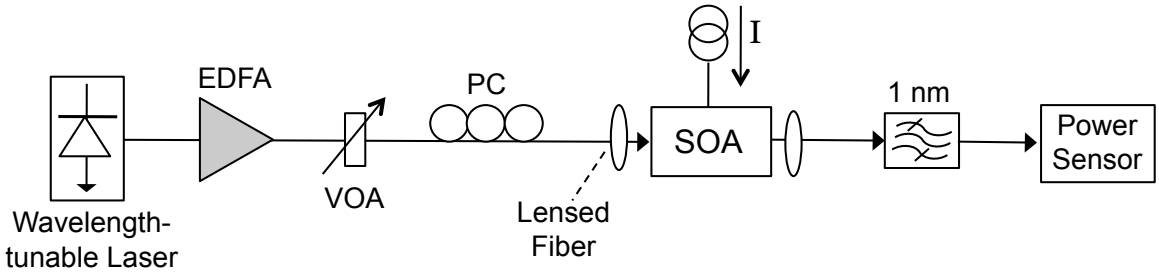


**Figure 4.3:** Experimental setup for measuring gain characteristics of hybrid silicon SOA. Device is pumped with 280 mA. A 1 nm optical filter is placed at the output to suppress ASE noise. EDFA: erbium-doped fiber amplifier, VOA: variable optical attenuator, PC: polarization controller

The measured amplifier gain for various silicon waveguide widths is shown in Figure 4.4 as a function of input power. The SOAs are pumped with 280 mA of current. System and facet losses are added back in order to find the on-chip gain characteristics. The decrease in gain for each device is a result of the saturation power of the gain medium, which depends on parameters, such as carrier lifetime and thickness of the active material [11]. Gain saturation can be understood intuitively by the fact that the power added to an optical signal cannot exceed the pump power. When the power in the active region becomes large, the carriers get depleted, thus reducing the gain. The input saturation power is defined as the input power at which the gain has decreased by 3 dB. The input saturation power can be analytically expressed by Eq. 4.2, where $P_s$ is the saturation parameter [14,17].

(3dB input saturation power) $$P_{in}^{sat} = \frac{P_s \cdot 2\ln 2}{G_o - 2} \tag{4.2}$$

(Saturation parameter) $$P_s = \frac{wdh\upsilon}{\Gamma a \tau} \tag{4.3}$$

$G_o$ is the small signal unsaturated gain, $w$ and $d$ are the dimensions of the quantum well, $\Gamma$ is the quantum well confinement factor, $a$ is the differential gain, and $\tau$ is the carrier lifetime. The gain characteristics in Figure 4.4 indicate that, as the Si waveguide decreases, the unsaturated gain increases. This is expected since the optical mode is more confined in the III-V active region. Consequently, with higher gain, the device reaches its limit faster, and the saturation power decreases. This is consistent with Eq. 4.2, where $P_s$ is inversely proportional to the quantum well confinement factor. Figures 4.5 and 4.6 summarize the unsaturated chip gain and the 3 dB input saturation power for each Si waveguide width. It shows that the 1.2 μm device has a good balance between the two.

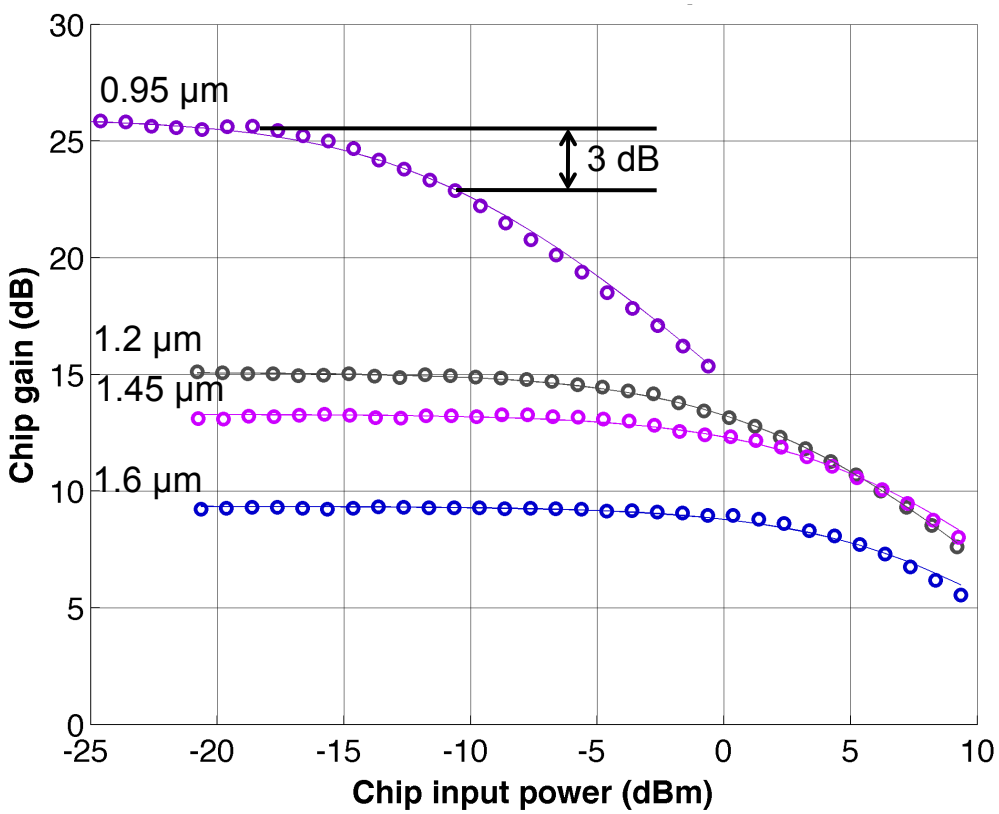


**Figure 4.4:** Measured gain saturation for various silicon waveguide widths by injecting a C-band light source. The pump current for each device is 280 mA.

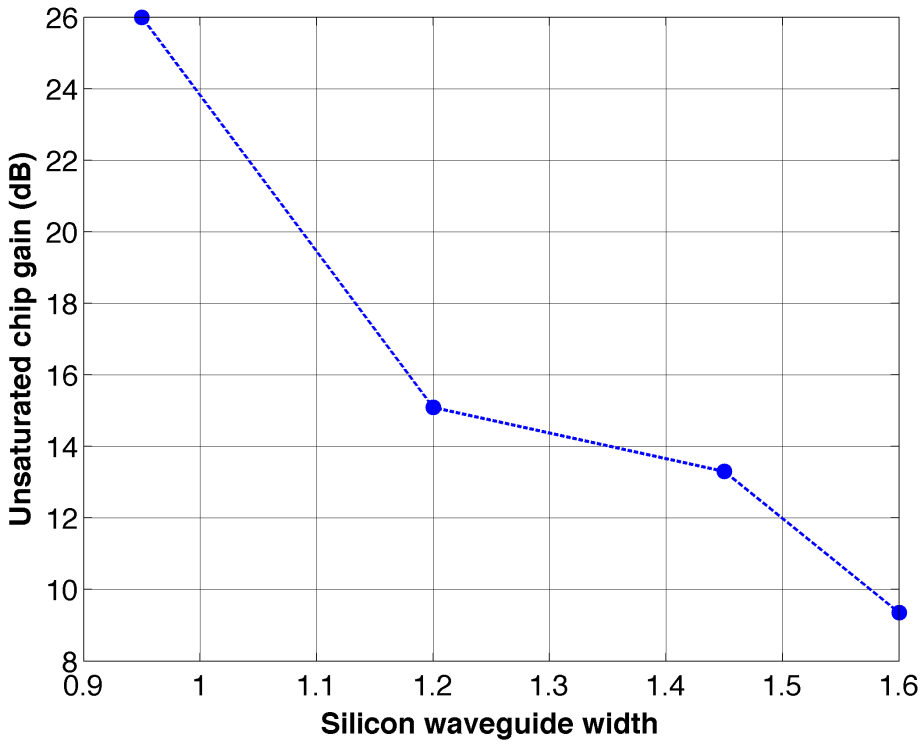


**Figure 4.5:** Measured unsaturated chip gain as a function of silicon waveguide width.

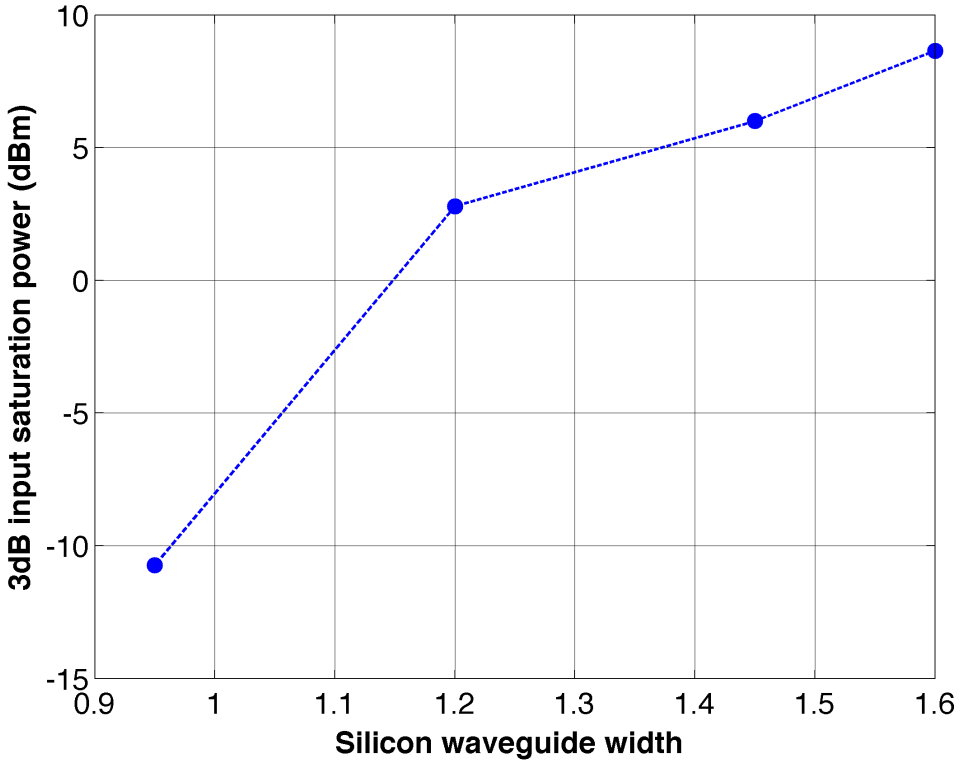


**Figure 4.6:** Measured 3dB output saturation power as a function of silicon waveguide width.

The average ASE noise level was measured at the output of the SOA (after the optical filter) with no input signal (Table 4.1). Multiplying by the photodiode's responsivity gives the ASE-induced current fluctuation [4]. For example, the 0.95 μm device has an average ASE noise level of -27.85 dBm, or 1.64 μW. The variance of the ASE-induced current fluctuation is then $2.2\times10^{-12}$ $A^2$ (Eq 4.4).

(Average ASE-induced current fluctuation for 0.95 μm device)

$$\begin{aligned}\left\langle i_{ASE}\right\rangle &= P_{ASE}R_d \\ &= \left(1.64\times10^{-6}\ \text{W}\right)\left(0.905\ \right. \\ &= 1.484\ \mu\text{A}\end{aligned} \tag{4.3}$$

(Variance of ASE-induced current fluctuation for 0.95 μm device)

$$\left\langle i_{ASE}^2\right\rangle = 2.2\times10^{-12}\ \text{A}^2 \tag{4.4}$$

In Section 3.2, the input-referred noise of the receiver without the optical amplifier was found to be $5.275\times10^{-12}$ $A^2$. With the 0.95 μm SOA inserted just before the photodiode, the average noise power would theoretically become $7.475\times10^{-12}$ $A^2$. Although the noise in the receiver increases, the input signal enhances by a factor of the SOA gain. The ratio of the electrical SNR with the amplifier to the SNR without the amplifier can be found by Eq. 4.5. Figure 4.7 plots the theoretical ratio value for each device using the measured unsaturated gain from Figure 4.5 and the measured average ASE noise level from Table 4.1. Although the 0.95 μm device shows the greatest improvement, this may not be the best choice because it has a short unsaturated gain region.

$$\frac{SNR}{SNR'} = \frac{R_d^2\left(GP_s\right)^2}{\sigma_{ASE}^2+\sigma_T^2}\left(\frac{\sigma_T^2}{R_d^2P_s^2}\right) = \frac{G^2\sigma_T^2}{\sigma_{ASE}^2+\sigma_T^2} \tag{4.5}$$

| Silicon waveguide width (μm) | Average ASE noise (dBm) |
|---|---|
| 0.95 | -27.85 |
| 1.2 | -34.87 |
| 1.45 | -38.73 |
| 1.6 | -40.83 |

**Table 4.1:** Measured average ASE noise level for various silicon waveguide widths

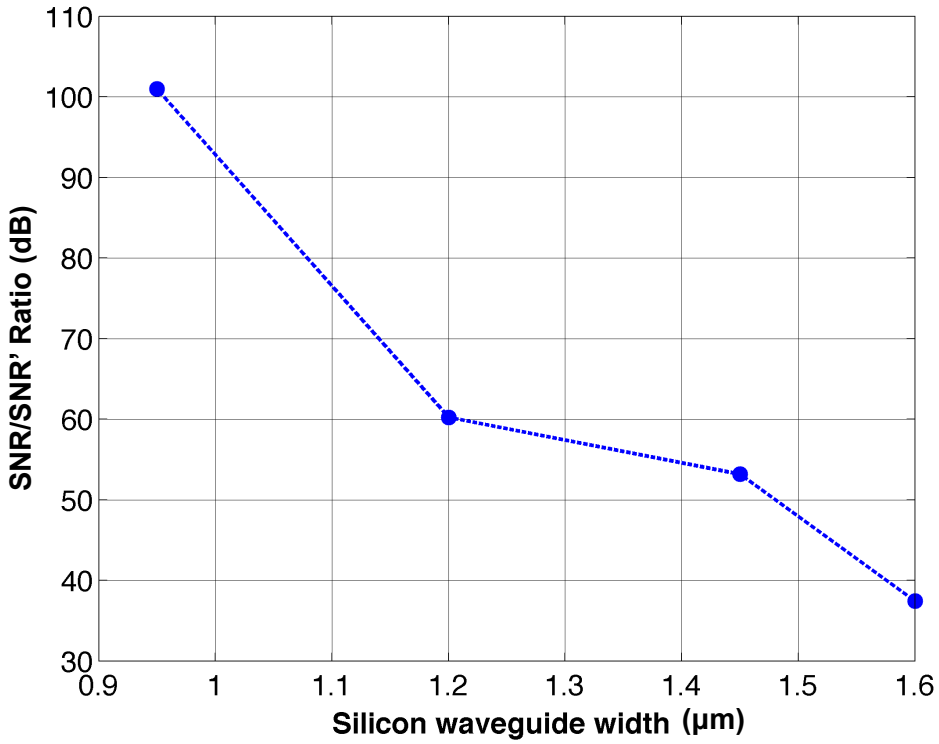


**Figure 4.7:** Theoretical ratio of electrical SNR with optical amplifier to SNR without optical amplifier. The SNR is taken at the input of the receiver, after the photodetection process.

## 4.4 Future Work

The gain characteristics presented were measured with continuous wave (CW) input power. If integrated in the OTDR scheme, the SOA would be detecting short pulses of light.

Therefore, the next experiment should investigate the amplification of pulsed light. It is important to note that the gain in an SOA is a function of unsaturated gain and time, and different parts of the pulse experience different amplification [11]. As a result, the pulse shape is altered after traveling through the amplifier. For example, the pulse may have a faster rise time than the trailing edge [6-7]. In an OTDR, the preservation of pulse shape and width are important for distinguishing between two discrete reflection peaks.

The gain of an SOA also depends on the optical mode confinement factor, which is different for TE and TM polarized light [15]. For randomly polarized light, such as the back-scattered pulse in an OTDR measurement, the amplitude will be distorted. Efforts have been made in SOA designs to eliminate polarization dependence, such as straining the active region [12,16]. Polarization sensitivity as low as 0.2 dB for 1550 nm optical signals have been achieved [5]. Another way to deal with the polarization sensitivity is to polarize the light before it reaches the SOA. This is achieved by splitting the light into its two polarizations, which are perpendicular to each other, rotating one of the polarizations, and adding them back together. Both polarizing beam-splitters and polarization rotators are commercially available. Additionally, polarization splitter and rotating devices have been built on silicon-on-insulator platforms [13].

# References


[1] M. A. Green and M. J. Keevers, "Optical-Properties of Intrinsic Silicon at 300 K," *Progress in Photovoltaics*, vol. 3, iss. 3, pp. 189-192, Jan 2007. [Online]. Available: http://onlinelibrary.wiley.com/doi/10.1002/pip.4670030303/abstracthttp://onlinelibrary wiley.com/doi/10.1002/pip.4670030303/pdf

[2] H. Park, A. W. Fang, J. E. Bowers, R. Jones, and O. Cohen, "An electrically pumped hybrid silicon evanescent amplifier," *OSA Technical Digest Series,* 2007. [Online]. Available: http://ieeexplore.ieee.org/stamp/stamp.jsp?arnumber=4348775

[3] H. Park, "Silicon Evanescent Devices for Optical Networks and Buffers," Ph.D. dissertation, Dept. Electrical and Computer Engineering, University of California, Santa Barbara, 2008.

[4] G. P. Agrawal, *Fiber-optic Communication Systems,* 4th ed., Hoboken, NJ: John Wiley & Sons, Inc., 2010.

[5] K. Morito, M. Ekawa, T. Watanabe, and Yuji Kotaki, "High-Output-Power Polarization-Insensitive Semiconductor Optical Amplifier," *Journal of Lightwave Technology,* vol. 21, no. 1, pp. 176-181, Jan. 2003. [Online]. Available: http://ieeexplore.ieee.org /stamp/stamp.jsp?arnumber=1190163

[6] P. P. Baveja, A. M. Kaplan, D. N. Maywar, and G. P. Agrawal, "Pulse amplification in semiconductor optical amplifiers with ultrafast gain-recovery times," *Proceedings of SPIE,* vol. 7598, Feb. 2010. [Online]. Available: http://www.researchgate.net/profile /Govind_Agrawal/publication/228924355_Pulse_amplification_in_semiconductor_opt al_amplifiers_with_ultrafast_gain-recovery_times/links/09e4150a447f00aa1f000000.pdf

[7] T. Arabadzhiev and I. Uzunov. "Amplification of an optical pulse sequence in semiconductor optical amplifiers," *Proceedings of SPIE,* vol. 5226, pp. 84-88, Nov. 2003. [Online]. Available: http://proceedings.spiedigitallibrary.org/proceeding. aspx?articleid=828739

[8] H. Liu, "Integrated Silicon Photonic Links for High Bandwidth Data Transportation," *OSA Technical Digest,* 2014. [Online]. Available: https://www.osapublishing.org /abstract.cfm?URI=OFC-2014-Th1D.1

[9] Z. Zhou, Z. Tu, T. Li, and X. Wang, "Silicon Photonics for Advanced Optical Interconnections," *Journal of Lightwave Technology,* vol. 33, no. 4, pp. 928-933, Feb. 2015. [Online]. Available: http://ieeexplore.ieee.org/stamp/stamp.jsp?arnumber =6977891

[10] B. Jalali, M. Paniccia, and G. Reed, "Silicon Photonics," *Microwave Magazine, IEEE,* vol. 7, iss. 3, pp. 58-68, Jun. 2006. [Online]. Available: http://ieeexplore.ieee.org.

proxy.library.ucsb.edu:2048/stamp/stamp.jsp?tp=&arnumber=1638290

[11] N. K. Dutta and Q. Wang, *Semiconductor Optical Amplifiers,* 5 Toh Tuck Link, Sangapore: World Scientific Publishing Co. Pte. Ltd., 2006. [Online]. Available: https://app.knovel.com/web/toc.v/cid:kpSOA00001/viewerType:toc/root_slug:semiconductor-optical/url_slug:kt0088V8YB

[12] L. Coldren, S. W. Corzine, and M. L. Masanovic, *Diode Lasers and Photonic Integrated Circuits,* 2nd, ed., Hoboken, NJ: John Wiley & Sons, 2012

[13] L. Liu, Y. Ding, K. Yvind, and J. M. Hvam, " Silicon-on-insulator polarization splitting and rotating device for polarization diversity circuits," vol. 19, iss. 13, pp. 12646-12651, Jun. 2011. [Online]. Available: https://www.osapublishing.org/view_article.cfm?gotourl=https%3A%2F%2Fwww.osapublishing.org%2FDirectPDFAccess%2F68F11D71-91A6-CB61-2842BD8E5DE8ACA6_218897%2Foe-19-13-12646.pdf%3Fda%3D1%26id%3D218897%26seq%3D0%26mobile%3Dno&org=

[14] E. J. Norberg, "Monolithically Integrated Reconfigurable Filters for Microwave Photonic Links," Ph.D. dissertation, Dept. Electrical and Computer Engineering, University of California, Santa Barbara, 2011.

[15] C. E. Webb and J. Jones, *Handbook of Laser Technology and Applications: Laser design and laser systems,* vol. 2, Bristol, United Kingdom: IOP Publishing Ltd, 2004.

[16] M. Itoh, Y. Shibata, T. Kakitsuka, Y. Kadota, and Y. Tohmori, "Polarization Insensitive SOA with a Strained Bulk Active Layer for Network Device Application," *IEE Phontonics Technology Letters,* vol. 14, no. 6, pp. 765-767, Jun. 2002. [Online]. Available: http://ieeexplore.ieee.org/stamp/stamp.jsp?arnumber=1003086

[17] A. Kapoor, E. K. Sharme, W. Freuda, and J. Leuthold. "Saturation characteristics of InGaAsP-InP bulk SOA," *Proc. Of SPIE,* vol. 7597, Feb. 2010. [Online]. Available: http://proceedings.spiedigitallibrary.org/proceeding.aspx?articleid=1338088

# Chapter 5

# Conclusion

## 5.1 Summary of Findings

This thesis reports on a high resolution OTDR that utilizes a compact and programmable ASIC. The ASIC fulfills the role of a tunable clock, pattern generator, precise timer, electrical receiver, and signal sampling circuit. Its features can be optimized for OTDR performance.

In this thesis, the ASIC-based OTDR is designed for single mode fiber testing. The ASIC's theory of operation was explained and its programmable settings were explored. The implemented OTDR successfully detects backscattered light pulses in a fiber with a PIN photodiode and 1 cm sampling resolution. The bandwidth of the receiver shows to be a limiting factor in the OTDR performance, which may be attributed to stray parasitics, such as those associated with the photodiode packaging. As a result, a pulse of short duration is slightly broadened when detected by the receiver. Nonetheless, the achievable spatial resolution of 3 cm is not far from its theoretical allowable spatial resolution (2 cm).

Also in analyzing the performance of the ASIC-based OTDR, the noise was measured at the output of the receiver. With repeated signal sampling and averaging, the RMS noise level can be reduced to 0.8969 mV. As a result, the signal-to-noise ratio at the output of the receiver can improve by 35.62 dBm. Furthermore, the receiver has a sensitivity of -39.88 dBm with 10,000 averages and a 2 nS wide transmission pulse. Widening the pulse, however, degrades the spatial measurement.

Lastly, a hybrid silicon semiconductor optical amplifier was considered for pre-amplification to the OTDR receiver. The gain and noise characteristics were measured to find its theoretical implications on the OTDR system. With increasing silicon waveguide widths, the on-chip unsaturated gain ranges from 26 dB to 9.35 dB. On the other hand, the 3 dB input saturation power varies from -10.74 dBm to 8.649 dBm. Although the SOA contributes to the noise in the receiver through amplified spontaneous emission, the gain may be sufficient to enhance the sensitivity of the receiver. Further experimental work is necessary in terms of integrating the SOA with the ASIC-based OTDR.

## 5.2 Other Applications

The capabilities offered by the OTDR ASIC can be extended to other applications. This section provides an overview of how the ASIC can be used for photon counting OTDR and fiber Bragg grating temperature sensing.

### Photon Counting OTDR

Photon counting OTDR was briefly discussed in Section 3.4. To review, it utilizes a Geiger mode avalanche photodiode (APD), which is biased above its breakdown voltage and

is capable of detecting single photons. One of the challenges faced with Geiger mode APDs is dead-zone elimination. Dead-zones are caused by charges getting trapped in the APD, which can result in an unwanted extra avalanche [2-3]. One way to eliminate dead zones is to employ a fast optical shutter to the APD, which would "blind" the APD outside the detection period, and therefore, prevent charge trapping.

The OTDR ASIC presented in this thesis offers the precise timing and pulse generation to implement photon counting OTDR with an optical shutter. The proposed OTDR scheme is shown in Figure 5.1 with two OTDR ASICs in parallel. The first produces the transmission pulse through external modulation, which is launched into the test fiber. The second provides the optical shutter. The additional clock and timing generation is used to synchronize the two ASICs. It should be noted that typically external modulators are polarization sensitive. Therefore, the backscattered signal would need to be polarized prior to the external modulator.

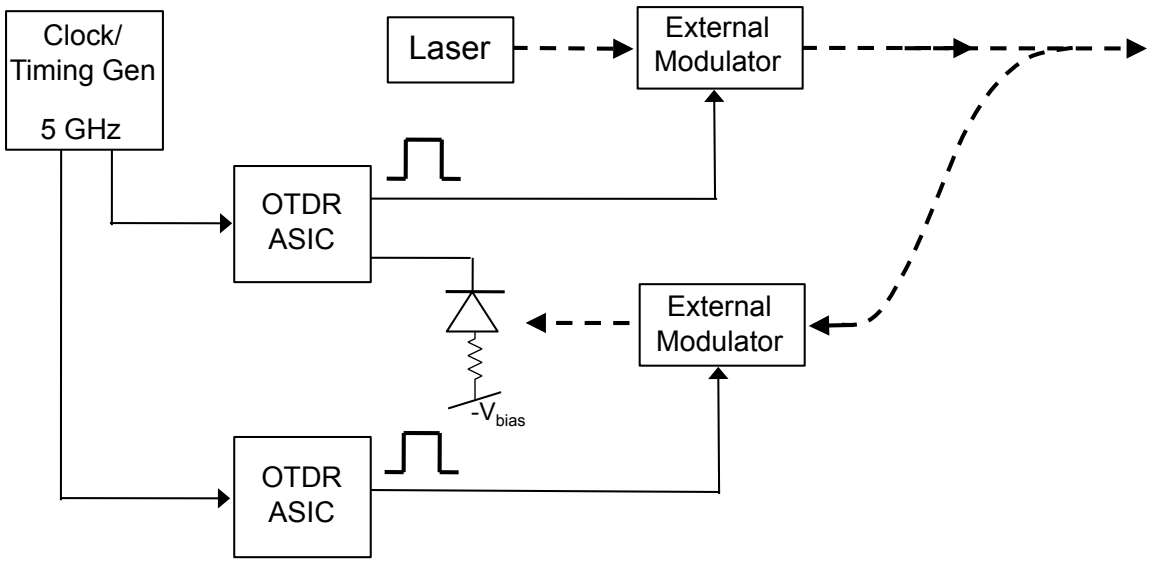


**Figure 5.1:** Proposed photon counting OTDR scheme with optical shutter. The dotted lines represent the optical signal paths.

## Fiber Bragg Grating Temperature Sensor

A fiber Bragg grating is a region of periodic variation in refractive index inscribed in the core of an optical fiber [4]. It reflects the propagating optical signal at particular wavelengths and transmits all others. The wavelength with strongest reflectivity depends on the Bragg grating period, temperature, and mechanical strain. Thus, Bragg gratings can be used in temperature and strain sensing applications. The ASIC-enabled temperature (or strain) sensor would be a similar setup to the OTDR presented in Chapter 2. Additional coding is needed to sweep the wavelength of a tunable laser so that an OTDR measurement is done at each wavelength. The data processing would entail finding the wavelength at which the strongest reflection occurred, and then determining the corresponding strain or change in temperature. The wavelength of a fiber Bragg grating sensor is related to strain and temperature by Eq. 5.1 [4].

$$\frac{\Delta\lambda}{\lambda_0} = k \cdot \varepsilon + \alpha_\delta \cdot \Delta T \tag{5.1}$$

$\Delta\lambda$ = wavelength shift
$\lambda_0$ = transmission wavelength
$k$ = gage factor
$\varepsilon$ = strain
$\alpha_\delta$ = change in refractive index
$\Delta T$ = change in temperature

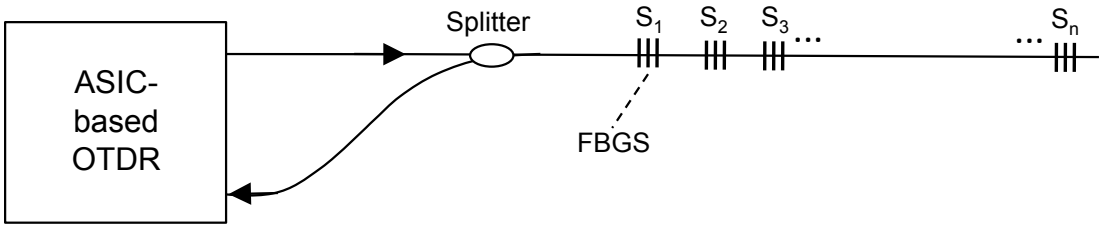


**Figure:** ASIC-based OTDR in fiber Bragg grating sensor (FBGS) application.

# References


[1] B. F. Aull, A. H. Loomis, D. J. Young, R. M. Heinrichs, B. J. Felton, P. J. Daniels, and D. J. Landers, "Geiger-Mode Avalanche Photodiode for Three-Dimensional Imaging," *Lincoln Laboratory Journal,* vol. 13, no. 2, pp 335-350, 2002. [Online]. Available: https://www.ll.mit.edu/publications/journal/pdf/vol13_no2/13_2 geigermode3d.pdf

[2] P. Eraerds, M. Legre, J. Zhang, H. Zbinden, and N. Gisin, "Photon Counting OTDR: Advantages and Limitations," *Journal of Lightwave Technology,* vol. 28, no. 6, pp. 952-964, Mar. 2010. [Online]. Available: http://ieeexplore.ieee.org/stamp/ stamp.jsp?arnumber=5371875

[3] F. Scholder, J. Gautier, M. Wegmuller, and N. Gisin, "Long-distance OTDR using photon counting and large detection gates at telecom wavelength," *Optics Communications,* vol. 213, pp. 57-61, Sept. 2002 [Online]. Available: http://ac.els-cdn.com/S0030401802020539/1-s2.0S0030401802020539main.pdf?_tid=a87dc5fe-074a-11e5-b47700000aab0f6b&acdnat=1433045474_cd45ea6dc4783d9107 ed20a6f6b947b2

[4] K. O. Hill and G. Meltz, "Fiber Bragg Grating Technology Fundamentals and Over view," *Journal of Lightwave Technology,* vol. 15, no. 8, pp. 1263-1276, Aug. 1997. [Online]. Available: http://ieeexplore.ieee.org/stamp/stamp.jsp?arnumber=618320

[5] M. Kreuzer, "Strain Measurement with Fiber Bragg Grating Sensors," [Online]. Available: http://micronoptics.ru/uploads/library/documents/FBGS_StrainMeasure ment_mo.pdf

# Appendix A

# Details of OTDR Scheme

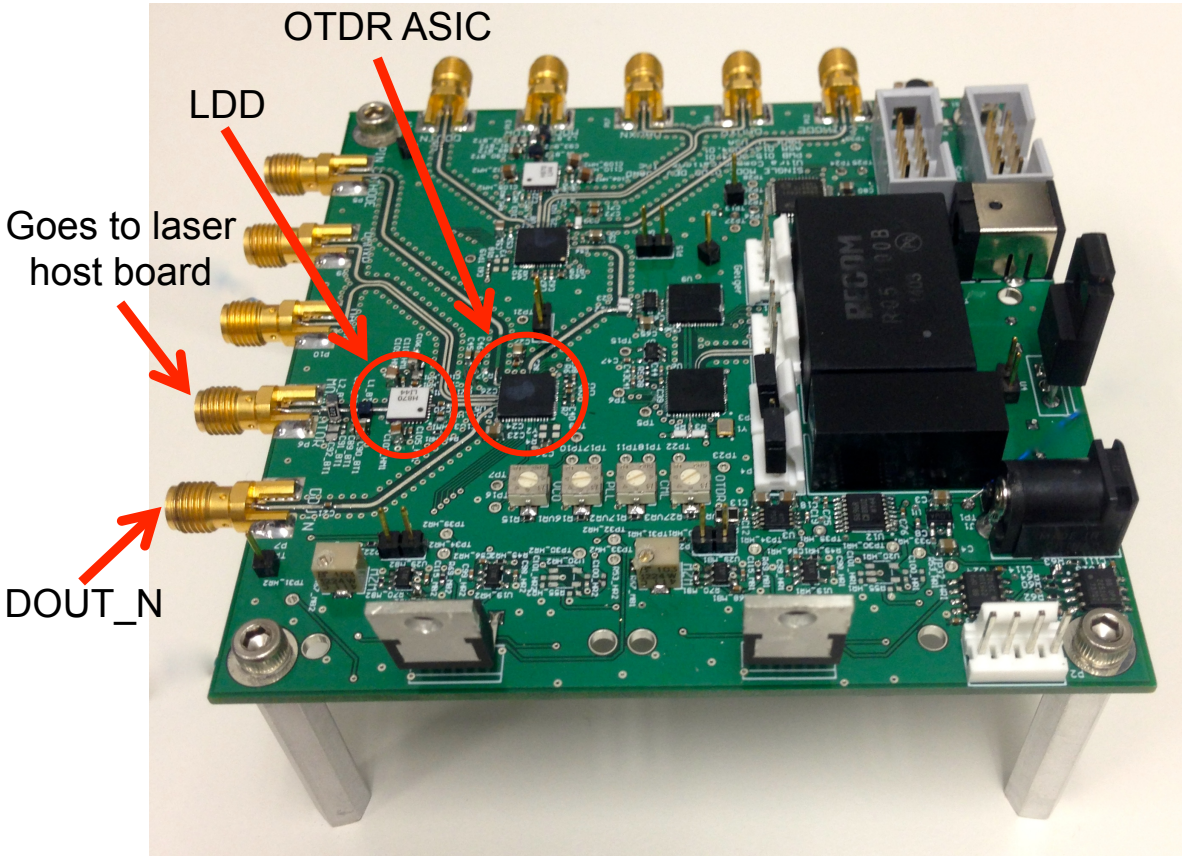


**Figure:** Host board for OTDR ASIC, laser diode driver (LDD), and photodiode. All high-speed traces have 50 Ω impedance. The output of the LDD connects to the laser host board via a SMA connector and 50 Ω cable. DOUT_N is the negative CML differential output of the ASIC; it is used as a trigger for the high-speed scope in Appendix B.

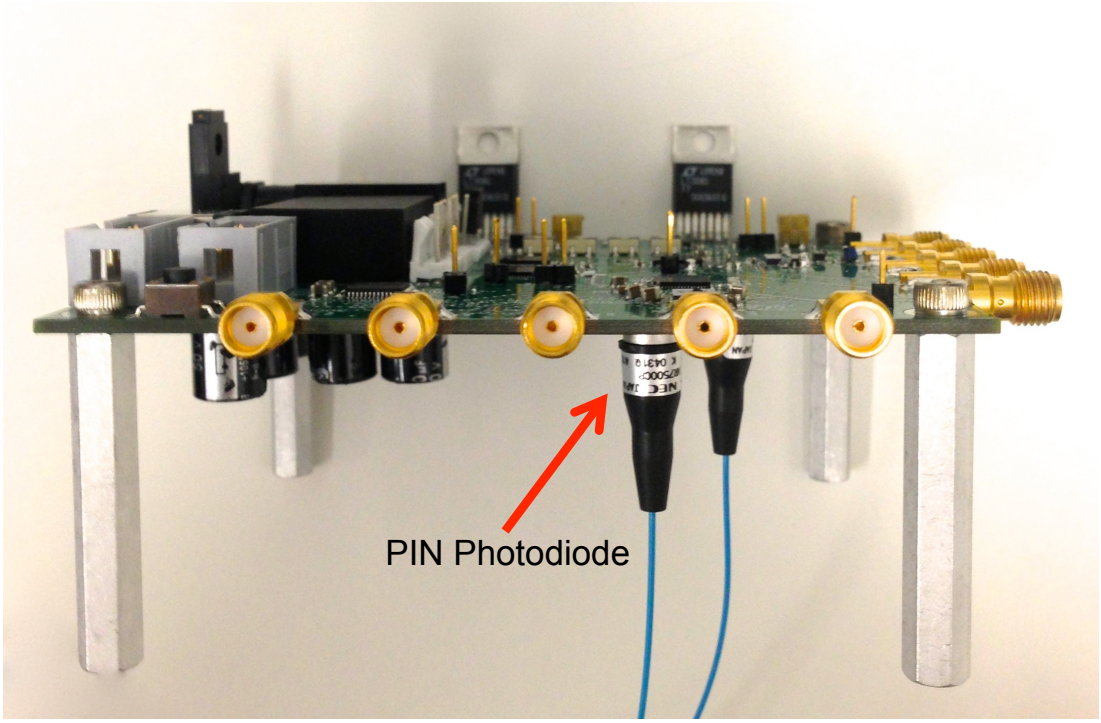


**Figure:** Side view of OTDR host board. Photodiode is mounted from the bottom and placed in close proximity to the OTDR chip.

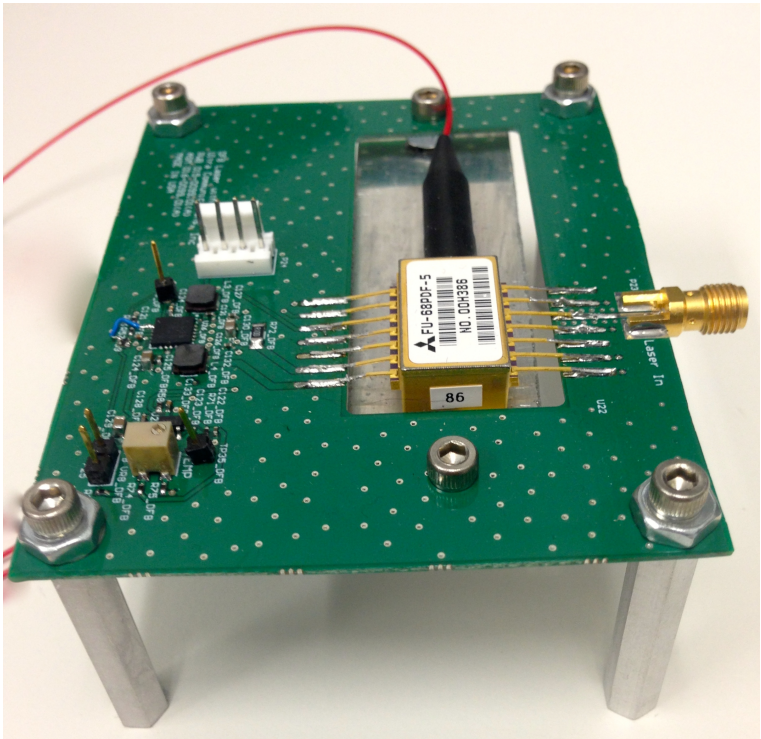


**Figure:** Host board for DFB laser diode module and thermoelectric cooling circuitry. A heatsink is attached to bottom of laser module to facilitate cooling.

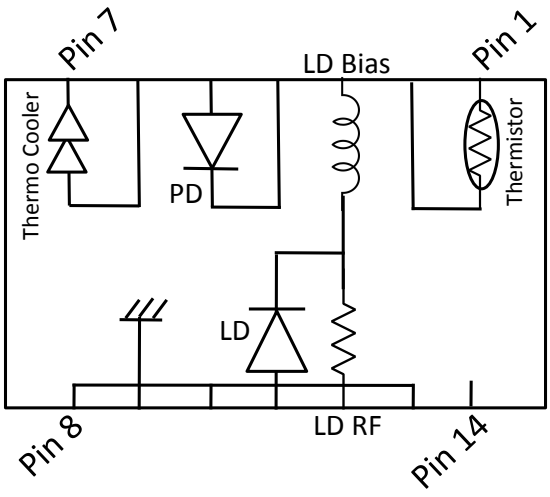


| Pin | Function |
|---|---|
| 1 | Thermistor |
| 2 | Thermistor |
| 3 | LD Bias (-) |
| 4 | PD Anode |
| 5 | PD Cathode |
| 6 | Cooler Anode |
| 7 | Cooler Cathode |
| 8 | GND |
| 9 | GND |
| 10 | NC |
| 11 | LD Anode, GND |
| 12 | LD RF Modulation |
| 13 | LD Anode, GND |
| 14 | NC |

**Figure (left):** Circuit diagram of laser diode module [1]. **Table (right):** Pin description for laser diode module.

# References

[1] Mitsubishi, "1.55 μm DFB-LD Module with Polarization Maintaining Fiber Pigtail," FU-68PDF-V510MxxB datasheet. [Online]. Available: http://pdf1.alldatasheet.com/datasheet-pdf/view/634/MITSUBISHI/FU-68PDF-V510MXXB.html

[2] Hittite Microwave Corporation, " MZ Optical Modulator Driver, DC-20 GHz," HMC870LC5 datasheet, v.05.0614. [Online]. Available: https://www.hittite.com/content/documents/data_sheet/hmc870lc5.pdf

# Appendix B

# Lab Equipment Used for Measurements

## High-speed Oscilloscope

The Digital Communication Analyzer (DCA) 86100 by Keysight Technologies [1].

- Minimum delay: 24 nS
- Trigger bandwidth: DC to 3.2 GHz
- Trigger sensitivity: 200 pS minimum pulse width
- Trigger impedance: 50 Ω

## 12.5 Gb/s Multimode Fiber-Optic Receiver Module by Picometrix

Fiber-coupled, PIN optical receiver with integrated transimpedance (TIA) in an 8-pin coaxial package with SMA output [2].

- Wavelength range: 760 – 1650 nm
- Responsivity: 0.95 A/W at 1550nm, single mode
- Conversion gain: 430 V/W at 1550 nm, single mode
- Bandwidth: 8.5 GHz

## References

[1] Keysight Technologies, "Wide-Bandwidth Oscilloscope Mainframe and Modules," Infiniium DCA-X 86100D datasheet, May 2015. [Online]. Available: http://literature.cdn.keysight.com/litweb/pdf/5990-5824EN.pdf?id=1909709

[2] Picometrix, LLC, PT-12B datasheet, Oct. 2009. [Online]. Available: http://sphotonics.ru/PT-12B.pdf

# Appendix C

# Matlab Scripts

### Frequency Response Estimate

```
%% Impulse Response Signal and Parameters
h = testdata; % OTDR measurement, which approximates receiver's impulse %
% response
Ts = 100e-12;       % Sampling Period
Fs = 1/Ts;     % Sampling rate
t = (0:(length(h)-1))*Ts; % time axis, where h is the impulse response


%% FFT Estimate of Transfer Function
Nfft = length(h);    % Number of fft points (setting this to a hire number
% will zero pad signal)
H = fft(h,Nfft);       % Fourier Transform of Data
fdiv = Fs/Nfft;      % Frequency Resolution
fk = ( (-Nfft/2+1):(Nfft/2) )*fdiv;   % Frequency Axis
H = fftshift(H);    % Shifts Aliasing Frequencies to negative frequency
H_dB = 20*log10( abs(H) );   % Magnitude Spectrum of Transfer Function
H_dB = H_dB – max(H_dB); % Normalize

%% Measured Impulse Response
figure(1);
plot(time,h,'linewidth',2);
xlabel('Time (nS)');
ylabel('Magnitude (V)','fontsize',16,'fontweight','bold');

%% FFT Estimate of Transfer Function
figure(2);
semilogx(fk*1/1e6,H_dB,'linewidth',1.2) % plot Spectrum vs. MHz
xlabel('Frequency (MHz)','fontsize',16,'fontweight','bold');
ylabel('Magnitude (dB)','fontsize',16,'fontweight','bold');
```

### Filtering

```
%% First compute frequency response of receiver
h = testdata; % OTDR measurement, which approximates receiver's impulse
%response
Ts = 100e-12;       % Sampling Period
Fs = 1/Ts;     % Sampling rate
t = (0:(length(h)-1))*Ts; % time axis, where h is the impulse response

Nfft = length(h);    % Number of fft points (setting this to a hire number
% will zero pad signal)
```

```
H = fft(h,Nfft);        % Fourier Transform of impulse response

%% Generate pulse and compute Fourier transform
T = 2e-9; % width of rectangular input pulse
d = 5e-9; % offset pulse
input_signal = rectpuls(t-d,T); % input signal, rectangular pulse with
%width, T, unity amplitude, and centered about d

H2 = fft(input_sig,Nfft);       % Fourier Transform of input signal

%% Multiply the two in frequency domain and compute inverse Fourier
filtered_output = ifft(H2.*H); % Filter data with transfer function H

plot(t,real(filtered_output));
```